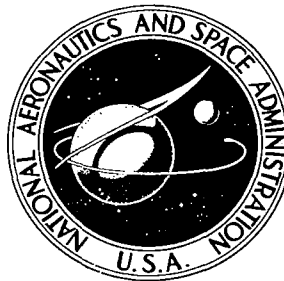


**NASA CONTRACTOR
REPORT**

NASA CR-1738



NASA CR-1738
C.1

0060797



**LOAN COPY: RETURN TO
AFWL (DOGL)
KIRTLAND AFB, N. M.**

**FLOW FIELDS OVER SHARP
EDGED DELTA WINGS
WITH ATTACHED SHOCKS**

by S. A. Powers and E. R. Beeman, Jr.

Prepared by
NORTHROP CORPORATION, AIRCRAFT DIVISION
Hawthorne, Calif.
for Langley Research Center





0060797

1. Report No. NASA CR-1738	2. Government Accession No.	3. Recipient's Catalog No.	
4. Title and Subtitle FLOW FIELDS OVER SHARP EDGED DELTA WINGS WITH ATTACHED SHOCKS		5. Report Date April 1971	
		6. Performing Organization Code	
7. Author(s) S. A. Powers and E. R. Beeman, Jr.		8. Performing Organization Report No.	
9. Performing Organization Name and Address Northrop Corporation Aircraft Division Hawthorne, California		10. Work Unit No. 722-01-10-06-23	
		11. Contract or Grant No. NAS1-7850	
12. Sponsoring Agency Name and Address National Aeronautics and Space Administration Washington, D. C. 20546		13. Type of Report and Period Covered Contractor Report	
		14. Sponsoring Agency Code	
15. Supplementary Notes			
16. Abstract <p>The problem of supersonic and hypersonic flow of an inviscid ideal gas over conical wings with sharp leading edges and attached shock waves has been treated using the Three-Dimensional Method of Characteristics. Solutions for both the expansion and compression side have been developed and provided as highly automated computer programs. These programs provide for wing cross sections of flat plate, modified wedge, or general conic shapes. Since the flow fields on upper and lower surfaces are independent the total wing shape can be a combination of any two of these three shapes. These solutions require from one to three minutes on a CDC 6600, and provide an accurate description of the flow field between the body and the external boundary (the shock wave on the compression side and the free stream on the expansion side). Results from these programs are compared with experimental and theoretical data.</p>			
17. Key Words (Suggested by Author(s)) Conical flow, Delta wing, Three-dimensional Method of Characteristics, Flow field		18. Distribution Statement Unclassified - Unlimited	
19. Security Classif. (of this report) Unclassified	20. Security Classif. (of this page) Unclassified	21. No. of Pages 66	22. Price* \$3.00

SYMBOLS

A	projected wing area
A_i, B_i, C_i, D_i	coefficients in the finite difference compatibility equation
b	local span
B	bluntness factor in the general conic equation
$B_i^{(J)}$	the i th body point on surface (J) . When i or (J) is omitted, their value is not significant to the discussion
C	root chord
C_D	drag coefficient, $\frac{\text{Drag}}{QA}$, where Q is the dynamic pressure and A the wing area
C_L	lift coefficient, $\frac{\text{Lift}}{QA}$
$C_{M_{\text{APEX}}}$	pitching moment coefficient about the wing apex, $\frac{\text{Moment}}{QAC}$
C_X	axial force coefficient, $\frac{\text{X-Force}}{QA}$
C_Y	normal force coefficient, $\frac{\text{Y-Force}}{QA}$
f	residual of gradient equation
$F_i^{(J)}$	the i th field point on surface (J)
F, F_1, F_2, F_3	wing surface equations
F_X, F_Y, F_Z	components of the normal to the wing surface
g	residual of compatibility equations
grad	$\frac{\partial}{\partial x} + \frac{\partial}{\partial y} + \frac{\partial}{\partial z}$, gradient operator
K	safety factor multiplier in the field point addition test
L	length along a bicharacteristic

m	counter
M	Mach number
\bar{N}	a unit vector perpendicular to the \bar{L} vector along a bicharacteristic
\bar{N}_B	unit vector normal to the body
\bar{N}_S	unit vector normal to the shock
N_X, N_Y, N_Z	components of unit normal vector
n	exponent in IVS shock shape equation, Equation (36)
n_1	resultant component normal to the leading edge formed by the X and Z components of the body surface normal vector
P	local static pressure. The units are not significant unless given
\bar{P}	position vector of a point relative to the apex of the wing (i.e., the origin of the coordinate system)
P_t	total pressure
Q	free stream dynamic pressure
R	local radius of curvature in the $Y=0$ plane; also, local radius of the wedge peak modification
S	incremental distance along a streamline
\bar{S}	streamline vector (See Equation (29))
$S_i^{(J)}$	the i th shock point on the surface (J)
\mathcal{J}	entropy
t	local thickness of the wing, measured in the Y direction
u_i	local velocity components
U_i	free stream velocity components

u, v, w	Cartesian components of the local velocity vector
V_{\max}	maximum possible velocity
\overline{V}_2	local velocity vector just behind shock wave
\overline{V}	free stream velocity vector
X, Y, Z	Cartesian coordinates in a right-handed system fixed to the apex of the wing. The X direction is along the wing centerline, Y is normal to the plane defined by the wing leading edges, and Z is spanwise
α	angle of attack
β_{shock}	shock wave angle, measured from the incident stream direction
γ	ratio of specific heats
δ	angle which locates position of bicharacteristics around Mach cone
η	streamline deflection angle across a shock wave
θ	angle between local velocity vector and Y axis (See Sketch 2)
θ	leading edge thickness angle, measured in the $X = \text{constant}$ plane
μ	Mach angle = arcsine $(1/M)$
λ	integration variable
Λ	leading edge sweep back angle
σ	shock wave angle in an $X = \text{constant}$ plane
ϕ	integration variable
ψ	angle between the local velocity vector and the $Z = 0$ plane (See Sketch 2)

Subscripts:

c	conditions at point being calculated
i	conditions at point i
n	normal component
p	parallel component

T	total , also thickness
∞	free stream condition
Superscripts:	
$(\bar{})$	vector quantity
$*$	specialized values (defined in text)
$(^{\wedge})$	quantities nondimensionalized by the span, b
(\sim)	average quantities
$i, i-1, i+1$	iteration sequence numbers

FLOW FIELD OVER SHARP EDGED DELTA WINGS WITH ATTACHED SHOCKS

by S.A. Powers and E.R. Beeman, Jr.
Northrop Corporation, Aircraft Division

SUMMARY

The problem of supersonic and hypersonic flow of an inviscid ideal gas over conical wings with sharp leading edges and attached shock waves has been treated using the Three-Dimensional Method of Characteristics. Solutions for both the expansion and compression side have been developed and provided as highly automated computer programs. These programs provide for wing cross sections of flat plate, modified wedge, or general conic shapes. Since the flow fields on upper and lower surfaces are independent the total wing shape can be a combination of any two of these three shapes. These solutions require from one to three minutes on a CDC 6600, and provide an accurate description of the flow field between the body and the external boundary (the shock wave on the compression side and the free stream on the expansion side). Results from these programs are compared with experimental and theoretical data.

INTRODUCTION

The supersonic and hypersonic flow fields about conical wings have been studied both experimentally and theoretically for a number of years. The exact analysis of conical flows has tempted a number of people into trying various methods, since such flows are mathematically two-dimensional. At the start of the work reported herein only two exact analyses were known, that of Fowell (Reference 1) and Babaev (Reference 2). Near the end of this project the works of Voskresenski and South and Klunker were published (References 3 and 4, respectively). These constitute the body of exact solutions available for comparison with the method discussed here.

The present approach is to use a third spatial dimension in the problem, along with the exact boundary conditions, and apply the Northrop developed Three-Dimensional Method of Characteristics (3DMoC). The 3DMoC program starts the calculation of the flow field from an approximate Initial Value Surface, and continues the calculation downstream until the resulting flow field becomes conical. This is similar to the use of time-dependent solutions now being applied to a number of problems.

The three-dimensional method of characteristics used in this work is a progressive development of the method used in References 5 and 6. A recent survey of three-dimensional methods is given in Reference 7. The present method, however, is not discussed in Reference 7, and differs from those discussed in Reference 7 in that it

- (a) calculates along true bicharacteristics, (not the projected bicharacteristics in a reference plane),
- (b) does not assume any type of distribution of variables, and
- (c) follows streamlines,

The present work is intended to provide essentially exact inviscid solutions of the flow fields about flat, wedge, and conic cross-section delta wings at angles of attack up to the point of shock wave detachment from the leading edge on the compression surface and for as large an angle of attack as possible on the leeward surface.

The results provided by the method presented here provide details of the pressure distribution, flow direction, and local Mach numbers throughout the flow field, as well as the strength and location of the external shock wave on the compression side.

The work was carried out by the Aerodynamics Research Branch, of the Northrop Corporation, Aircraft Division under Contract NAS1-7850 for the Langley Research Center, and has been assigned Northrop Number NOR-69-70 for purposes of internal control.

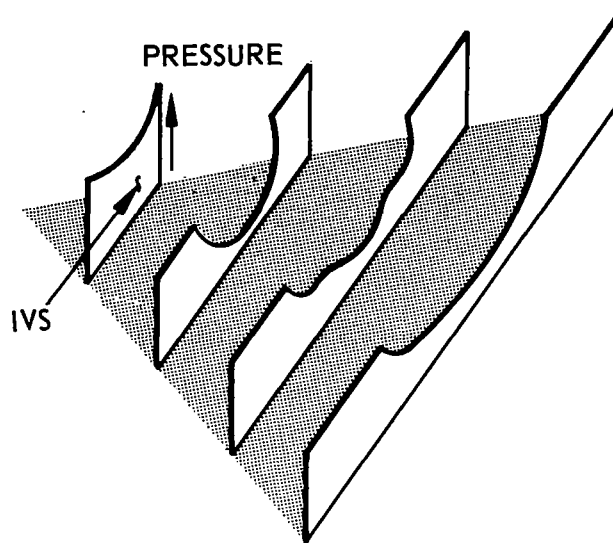
BASIC APPROACH

The method chosen for determining the conical flow over the upper and lower surfaces of both zero and finite thickness sharp edge delta wings is based on the well-known tendency for method of characteristics solutions to approach asymptotic limits. For example, the pressures far downstream on blunted cones asymptotically return to sharp cone values both experimentally and in rotationally symmetric methods of characteristic solutions. Thus, the method may be said to be "spatially asymptotic."

The present method starts with an approximate solution and continues the calculation until the results become conical. On a wing with a given geometric cross section shape an Initial Value Surface (IVS), consisting of points on the body and the shock where the flow properties are defined, is erected near the wing apex. The general Three-Dimensional Method of Characteristics solution then uses this IVS as its data surface and constructs a new data surface. This surface is then used as another IVS, and the process is repeated. The calculations are continued until the pressures on the wing centerline are constant to within an accuracy criterion specified by the user. The solution then has become self similar. Sketch 1 shows the development of such a solution. Depending upon the geometry of the wing's cross section, the angle of attack, and the free stream Mach number, the self similar solutions occur within 10 to 30 surfaces, or in one to three minutes on a CDC 6600 computer.

All calculations are carried out on constant X (constant body station) planes. Thus, each body, field and shock point will have the same values of X. This method offers several advantages over the conventional method of carrying out the solution along characteristics surfaces for the case of delta wing flow fields. Some of the advantages are:

1. Organization of the data is such that the results are easily interpreted.
2. The lengths of all the bicharacteristics for a given Mach conoid are approximately the same. This apparently removes the need for the weighting factors discussed in Reference (5).



Sketch 1

3. The problems associated with warped shock lines (if body lines are specified) or warped body lines (if shock lines are specified) are avoided.
4. The problems associated with step size control are greatly reduced.

The solution is started, in general, from an approximate set of body and shock points. As the solution progresses downstream field points are added as space for them becomes available. The solution continues until either the convergence criteria are satisfied or until the specified number of surfaces is calculated.

From experience it was found that convergence of a solution was indicated by the asymptotic approach to a constant value of the pressure on the body centerline. The program logic senses this asymptotic approach by calculating first and second differences of the body centerline pressures. The actual magnitude used for convergence is specified by the user, but values of 10^{-3} or 10^{-4} are recommended until sufficient user experience is gained to permit judgment based on needs.

Since this is an inviscid solution there is no absolute scale to the problem. The apex of the wing is located at the origin of the coordinate system, and the IVS is located at the downstream station $X = 1.0$. The user specifies the calculation step size, ΔX , to be used downstream of this station. The step size should not be so large

that the base points for calculating the second surface fall completely outside the shock wave, nor so small that a large number of field points are added very early in the calculation.

This calculation scheme follows streamlines. Once a streamline has been started, it is continued downstream until the problem is terminated. The program can be restarted from any surface. By using the restart option of the program, points can be thinned out. The program adds one body point and one shock point to each new surface, and as many field points as can be fitted between the shock and the body. The maximum number of body or shock points on any surface has been limited to 50, to keep the program core storage requirement down to a reasonable value.

This method sets the body surface entropy (i. e. , total pressure) equal to the value at the leading edge. The shock wave entropy distribution depends upon the local inclination of the shock wave surface. As the solution proceeds downstream the distance between the shock wave and the body increases until there exists sufficient room for field points to be added. The initial point on each field point streamline is located halfway between the upper and lower boundary data lines (these are initially the shock and body lines, but later become field and shock lines). The properties, including the entropy, are then determined by interpolation. Although strictly speaking this process introduces an error, the results are more than sufficient for engineering accuracy since the rates of change of the total pressure distribution are usually greatly reduced before the first field points are introduced (i. e. , the total pressure distribution is close to the converged values).

The gas model used here is that of an inviscid ideal gas with a fixed but arbitrary ratio of specific heats. Since the basic solution follows streamlines, the inclusion of real gas chemistry effects is essentially straightforward.

METHODS

The Governing Equation

The work discussed here, the application of the three-dimensional method of characteristics (3DMoC) solution to the problem of delta wings with attached shocks, is an extension of a method developed by Northrop and applied to the solution of flow fields about smooth bodies (Reference 5) and the interaction of multiple exhaust jets (References 6 and 8). This report discusses the specialization of the methods

given in Reference 5 for the treatment of sharp-edge delta wings with attached leading edge shocks.

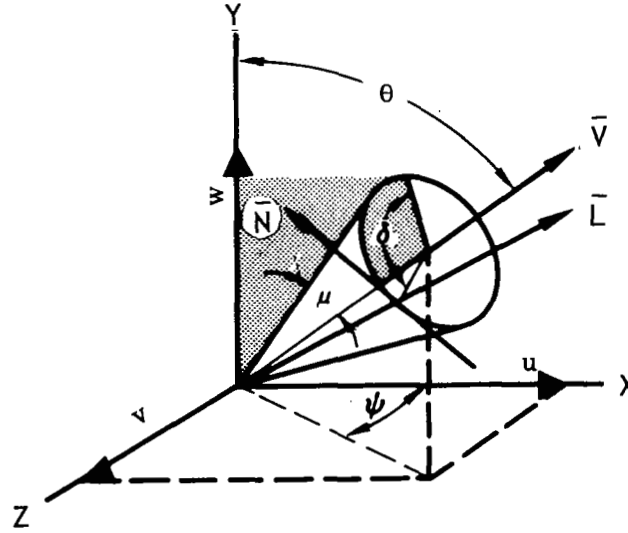
The general compatibility equation governing the properties along bicharacteristics is (Reference 5).

$$\frac{1}{\gamma P} \frac{\partial P}{\partial L} - \frac{\cos \delta}{\sin \mu \cos \mu} \frac{\partial \theta}{\partial L} + \frac{\sin \theta \sin \delta}{\sin \mu \cos \mu} \frac{\partial \psi}{\partial L} + \frac{1}{\cos \mu} \left[\sin \delta \frac{\partial \theta}{\partial N} + \sin \theta \cos \delta \frac{\partial \psi}{\partial N} \right] = 0 \quad (1)$$

Along streamlines the isentropic condition is also a compatibility relation.

$$d\mathcal{J} = 0 \quad (2)$$

The angles θ , ψ , δ , μ are defined in sketch 2:



Sketch 2

Note that \bar{V} is the local velocity vector and μ is the semi-vertex angle of the infinitesimal Mach cone, or the Mach angle. The angles θ and ψ are the Euler angles defining the direction of the local velocity vector, and δ locates a specific bicharacteristic on the Mach cone. The vector \bar{L} is along a bicharacteristic and hence is one of the generators of the Mach cone. The vector \bar{N} is normal to \bar{L} .

The velocity components are related to \bar{V} , θ , and ψ by

$$u = |\bar{V}| \sin \theta \cos \psi \quad (3a)$$

$$v = |\bar{V}| \cos \theta \quad (3b)$$

$$w = |\bar{V}| \sin \theta \sin \psi, \quad (3c)$$

as can be seen from sketch 2 above.

The application of the three-dimensional method of characteristics requires solving Equation (1) for P , θ , ψ , given sufficient initial data and boundary conditions for the problem under consideration. Note that contrary to the rotationally-symmetric method of characteristics compatibility relation, Equation (1) contains derivatives normal to the bicharacteristics, $\frac{\partial \theta}{\partial N}$ and $\frac{\partial \psi}{\partial N}$. Thus, the proper determination of a solution requires a sufficiently accurate determination of $\text{grad } \theta$ and $\text{grad } \psi$ which are used to determine the components of the gradients in the \bar{N} direction. The gradient of these two angles is determined in the following manner.

Let

$$\frac{\partial \theta}{\partial N} = \frac{\partial \theta}{\partial X} \frac{\partial X}{\partial N} + \frac{\partial \theta}{\partial Y} \frac{\partial Y}{\partial N} + \frac{\partial \theta}{\partial Z} \frac{\partial Z}{\partial N} \quad (4)$$

If we have m segments of bicharacteristics or other appropriate lines at the ends of which we know θ , the gradient, $\frac{\partial \theta}{\partial X}$, $\frac{\partial \theta}{\partial Y}$, $\frac{\partial \theta}{\partial Z}$ can be identified as the values which minimize the function

$$f = \sum_{i=1}^m \left[\Delta \theta_i - \Delta X_i \frac{\partial \theta}{\partial X} - \Delta Y_i \frac{\partial \theta}{\partial Y} - \Delta Z_i \frac{\partial \theta}{\partial Z} \right]^2 \quad (5)$$

where $\Delta \theta_i$ means the change in θ along a given finite length line (i.e., the geometric approximations to the bicharacteristics), ΔX_i the change in X , etc. The resulting three linear equations in three unknowns can be easily solved for $\frac{\partial \theta}{\partial X}$, $\frac{\partial \theta}{\partial Y}$, $\frac{\partial \theta}{\partial Z}$, the components of $\text{grad } \theta$. An identical operation is carried out for determining $\text{grad } \psi$.

Once $\text{grad } \theta$, $\text{grad } \psi$ are determined, Equation (1) can be expressed in finite difference form, and applied to bicharacteristics from three base points which intersect at the new point whose properties are to be determined. This process yields three equations for the three unknowns, P , θ , ψ at the new point. However, experience has shown (Reference 9) that by using more than the minimum number of bicharacteristics an improved solution can be obtained. This is due in part to improved symmetry in the location of the bicharacteristics. Letting the properties at a new point be denoted

by the subscript c, and the base points by the numbers 1 through 4, the basic finite difference form of the compatibility relation, Equation (1), is

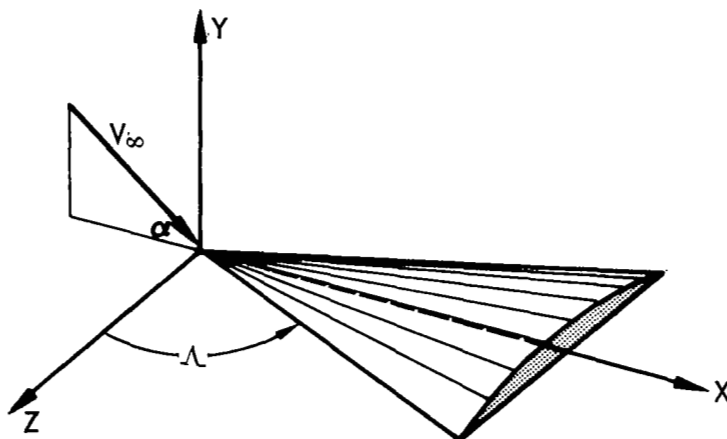
$$\begin{aligned} \frac{P_c - P_i}{r \tilde{P}} - \frac{\cos \delta_i}{\sin \tilde{\mu} \cos \tilde{\mu}} (\theta_c - \theta_i) + \frac{\sin \tilde{\theta} \sin \delta_i}{\sin \tilde{\mu} \cos \tilde{\mu}} (\psi_c - \psi_i) \\ + \frac{1}{\cos \tilde{\mu}} (\sin \delta_i \frac{\partial \theta}{\partial N_i} + \sin \tilde{\theta} \cos \delta_i \frac{\partial \psi}{\partial N_i}) \Delta L_i = 0 \end{aligned} \quad (6)$$

$i = 1, 2, 3, 4$

where the quantities with a tilde denote averages of properties at the base point and the new point. Note that δ_i , the bicharacteristic location angle, is unique for each bi-characteristic and therefore is not an average. The specialized application of Equation (6) will be discussed below in the sections covering the field point, body point, and shock point solutions.

Body Description

The wing is situated in a right-handed Cartesian coordinate system with the apex at (0, 0, 0) and the centerline extended along the positive X axis, as shown in sketch 3.



Sketch 3

The Y axis extends upward, and the Z axis spanwise. The wing thickness is on the positive side of the X-Z plane, and angle of attack vector lies in the X-Y plane and has a negative Y component for positive angle of attack. The wing sweepback, Λ , is measured from the Z axis.

Three types of cross sections are treated: Flat plate, modified wedge, and general conic. The body point subroutine of the three-dimensional method of characteristics program requires $Y = F_1(X, Z)$ and \bar{N} , the normal to the body surface at (X, Y, Z) . The components of \bar{N} are determined by

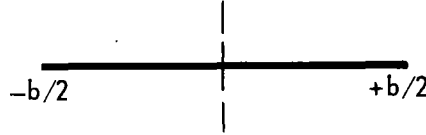
$$N_X = \frac{\partial F / \partial X}{|\text{grad } F|} \quad (7a)$$

$$N_Y = \frac{\partial F / \partial Y}{|\text{grad } F|} \quad (7b)$$

$$N_Z = \frac{\partial F / \partial Z}{|\text{grad } F|} \quad (7c)$$

where $F = F(X, Y, Z)$ is the equation of the body surface. The equation of the surface and the gradients for each geometry are given in the following, and the profiles are illustrated by sketches.

Flat Plate



Sketch 4

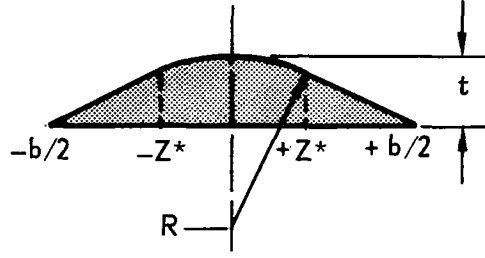
$$F_1(X, Y, Z) = Y = 0 \quad (8)$$

$$\partial F_1 / \partial X = 0 \quad (9a)$$

$$\partial F_1 / \partial Y = 1 \quad (9b)$$

$$\partial F_1 / \partial Z = 0 \quad (9c)$$

Modified Wedge



Sketch 5

The modified wedge has a cross section in which the sharp peak is replaced by a radius. The spanwise location of the wedge-radius junction is denoted by Z^* . The maximum thickness at the centerline is t ; and the angle between the wedge section and the $Y = 0$ is θ , measured in an $X = \text{constant}$ plane. The local radius R and thickness t are functions only of X . Since the geometry is conical, R/b and t/b are both constants.

In the outboard region, $Z^* \leq Z \leq b/2$

$$F_2(X, Y, Z) = Y - (X \cot \Lambda - Z) \tan \theta = 0 \quad (10)$$

$$\partial F_2 / \partial X = - \frac{\tan \theta}{\tan \Lambda} \quad (11a)$$

$$\partial F_2 / \partial Y = 1 \quad (11b)$$

$$\partial F_2 / \partial Z = \tan \theta \quad (11c)$$

In the inboard region, $0 \leq Z \leq Z^*$

$$F_2(X, Y, Z) = Y + \left[(R - t) - \sqrt{R^2 - Z^2} \right] = 0 \quad (12)$$

$$\frac{\partial F_2}{\partial X} = \left[\frac{-\hat{R}^2}{\sqrt{\hat{R}^2 - \hat{Z}^2}} + (\hat{R} - \hat{t}) \right] \frac{2}{\tan \Lambda} \quad (13a)$$

$$\frac{\partial F_2}{\partial Y} = 1 \quad (13b)$$

$$\frac{\partial F_2}{\partial Z} = \frac{\hat{Z}}{\sqrt{\hat{R}^2 - \hat{Z}^2}} \quad (13c)$$

where ($\hat{}$) refers to quantities nondimensionalized by the local span, b .

If \hat{R} and \hat{t} are given, then

$$\hat{Z}^* = \frac{\hat{R}^2 \pm \sqrt{\hat{R}^4 - 4 \left[1/4 + (\hat{R} - \hat{t})^2 \right] (2\hat{R} - \hat{t}) \hat{R}^2 \hat{t}}}{2 \left[1/4 + (\hat{R} - \hat{t})^2 \right]} \quad (14)$$

$$\theta = \arctan \frac{\hat{Z}^*}{\sqrt{\hat{R}^2 - \hat{Z}^{*2}}} \quad (15)$$

If \hat{R} and θ are given, then

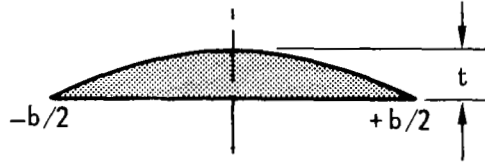
$$\hat{Z}^* = \hat{R} \sin \theta \quad (16)$$

$$\hat{t} = \hat{R} - \sqrt{\hat{R}^2 - \hat{Z}^{*2}} - (\hat{Z}^* - 1/2) \tan \theta \quad (17)$$

General Conic

The general conic equation is

$$Z^2 = 2R(t - Y) - B(t - Y)^2 \quad (18)$$



Sketch 6

With the local radius of curvature at the centerline, $\hat{R} = R/b$, or local centerline thickness, $\hat{t} = t/b$, specified

$$F_3(X, Y, Z) = Y + \left[\frac{R}{B} - t - \frac{\sqrt{R^2 - BZ^2}}{B} \right] = 0 \quad (19)$$

$$\partial F_3 / \partial X = \frac{2}{\tan A} \left[\frac{\hat{R}}{B} \left(1 - \sqrt{\hat{R}^2 - B\hat{Z}^2} \right) \right] - \hat{t} \quad (20a)$$

$$\partial F_3 / \partial Y = 1 \quad (20b)$$

$$\partial F_3 / \partial Z = \frac{\hat{Z}}{\sqrt{\hat{R}^2 - B\hat{Z}^2}} \quad (20c)$$

where if \hat{R} is specified

$$\hat{t} = \frac{\hat{R} - \sqrt{\hat{R}^2 - B/4}}{B} \quad (21)$$

or if \hat{t} is specified

$$\hat{R} = \frac{1 + 4B\hat{t}^2}{8\hat{t}} \quad (22)$$

For parabolic wings, $B = 0$, the above equations are invalid. From the basic equation, for $B = 0$, the relation between thickness and radius of curvature at the centerline is

$$\hat{R} \hat{t} = \frac{1}{8} \quad (23)$$

and the surface equation is

$$F_3(X, Y, Z) = Y - \left[\hat{t} - \frac{Z^2}{2\hat{R}} \right] = 0 \quad (24)$$

$$\partial F_3 / \partial X = \frac{-2}{\tan \Lambda} \left[\hat{t} + \frac{\hat{Z}^2}{2\hat{R}} \right] \quad (25a)$$

$$\partial F_3 / \partial Y = 1 \quad (25b)$$

$$\partial F_3 / \partial Z = \frac{\hat{Z}}{\hat{R}} \quad (25c)$$

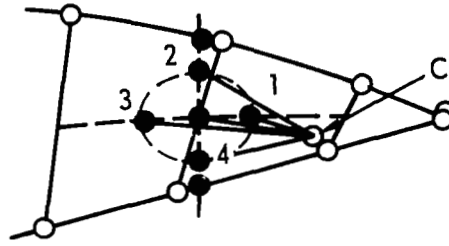
Field Point Solution

Two distinct aspects of the field point solution must be discussed; the solution of the compatibility equations given the base point properties, and the determination of the base points properties.

The solution of the compatibility equations, Equation (1) above, is determined in a least squares sense.* Given the four base points, 1, 2, 3, 4, shown in Sketch 7, the

*This least square solution was discovered and applied by the members of the Aerodynamic Research Department. However, upon reading Butler's paper (Reference 10) dated 1959, the authors found that he had proposed the same type of solution.

bicharacteristics C-1, C-2, C-3, C-4 are constructed and the solution obtained at C in a straightforward manner.



Sketch 7

The four equations are:

$$A_i P_c + B_i \theta_c + C_i \psi_c = D_i \quad i = 1, 2, 3, 4 \quad (26)$$

where $A_i = \frac{1}{\gamma \tilde{P}_i}$

$$B_i = -\frac{\cos \delta_i}{\sin \tilde{\mu}_i \cos \tilde{\mu}_i}$$

$$C_i = \frac{\sin \tilde{\theta}_i \sin \delta_i}{\sin \tilde{\mu}_i \cos \tilde{\mu}_i}$$

$$D_i = -\frac{1}{\cos \tilde{\mu}_i} \left[\sin \delta_i \frac{\partial \theta}{\partial N_i} + \sin \tilde{\theta}_i \cos \delta_i \frac{\partial \psi}{\partial N_i} \right] \Delta L_i \\ + \frac{P_i}{\gamma \tilde{P}_i} - \frac{\cos \delta_i}{\sin \tilde{\mu}_i \cos \tilde{\mu}_i} \theta_i + \frac{\sin \tilde{\theta}_i \sin \delta_i}{\sin \tilde{\mu}_i \cos \tilde{\mu}_i} \psi_i$$

In these equations a suffix i refers to a quantity associated with a particular base point, while a quantity with a tilde refers to an average of the value at the i th base point and the new point.

To find the minimum value of a residual of these compatibility equation, defined as

$$g = \sum_{i=1}^4 (A_i P_c + B_i \theta_c + C_i \psi_c - D_i)^2, \quad (27)$$

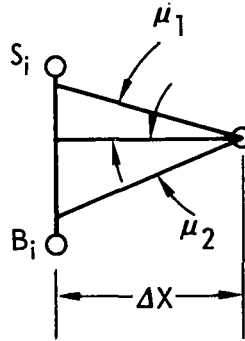
we differentiate with respect to P_c , θ_c , and ψ_c , and set the results equal to zero. We then have

$$\begin{bmatrix} \sum A_i^2 & \sum A_i B_i & \sum A_i C_i \\ \sum A_i B_i & \sum B_i^2 & \sum B_i C_i \\ \sum A_i C_i & \sum B_i C_i & \sum C_i^2 \end{bmatrix} \begin{bmatrix} P_c \\ \theta_c \\ \psi_c \end{bmatrix} = \begin{bmatrix} \sum A_i D_i \\ \sum B_i D_i \\ \sum C_i D_i \end{bmatrix} \quad (28)$$

This can easily be solved for P_c , θ_c , ψ_c . Note that the right hand side of Equation 28 contains θ_c and ψ_c implicitly in the grad θ , grad ψ calculations used to define $\frac{\partial \theta}{\partial N}$ and $\frac{\partial \psi}{\partial N}$. Since the solution is iterative, Equation 27 is truly minimized when θ_c and ψ_c no longer change values significantly from iteration to iteration.

Also note that the present solution no longer "weights" the solution of the bicharacteristic, as is done in Reference 5. This is due to the nearly equal length of the bicharacteristics used in the present solution.

The overall solution is initiated using only body and shock point. The distance between associated pairs of body and shock points is tested to see if sufficient room exists for the inclusion of the base of a field point Mach cone as in Sketch 8.



Sketch 8

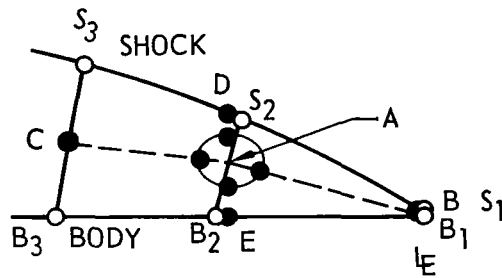
If ΔS , the distance between the shock and body points is greater than

$$K \Delta X (\tan \mu_1 + \tan \mu_2)$$

a field point is inserted. Here K as a multiplier is used to insure that sufficient space exists for the field point, and μ_1 , and μ_2 are the Mach angles at the upper and lower boundary points - shock and body points in this example. As the solution proceeds downstream the distance between the shock and field points increases just as the

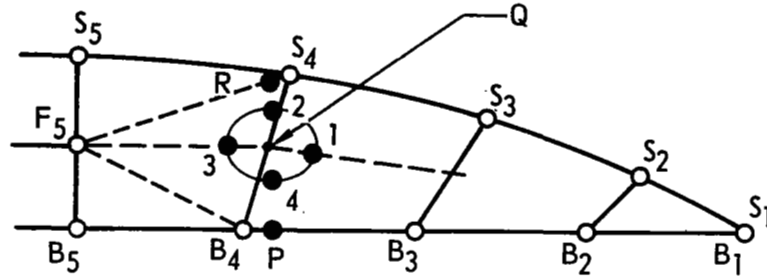
distance between shock and body points. When the test given above shows sufficient room exists, additional levels of field points are inserted. This usually occurs above already existing levels of field points.

The process of determining the base point properties and the origin of the stream-line for a newly added field point is illustrated with Sketch 9. If the distance between points S_2 , B_2 exceeds the criterion discussed above, an origin for the field point stream-line is defined as a point midway between points S_2 , B_2 ; point A in the sketch. The properties there are determined by linear interpolation between points S_2 , B_2 . In cases where no field points exist to one (or both) sides, the next adjacent pairs of shock and body points are used to define a location and properties at a point midway between them; points C and B. Similarly the spanwise location of point A is used to define properties at a point on the shock between points S_2 and S_3 , and on the body between points B_1 and B_2 . (In each case the correct pair of body/shock points is chosen to permit interpolation.) The resulting points are D and E. Base point 1 is now located on the line A-B and its properties are determined by interpolation. Similarly, base point 2 is located on A-D, point 3 on A-C and point 4 on A-E.



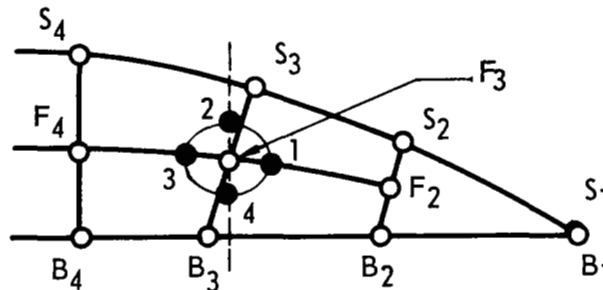
Sketch 9

When a base point is to be determined outboard of the end of a field line, a slightly specialized procedure must be invoked. In sketch 10, base points 2, 3, and 4 are to be located in the region outboard of the line of field points ending with F_5 . Base point 3 of course is easily located on this plane by interpolating along the line F_5 -Q, where Q is the midpoint of S_4 - B_4 . To prevent serious error propagation the properties of base point 2 must lie on the surface defined by the properties and locations of points S_4 , B_4 , and F_5 . This is easily accomplished by interpolating for a data point, R, on the line S_4 - F_5 , locating base point 2 on this line, and interpolating between points R and Q for the associated properties. No such problem exists with base point 4 since an interpolated data point can be located between B_3 and B_4 .



Sketch 10

In the case of a field point added onto an already existing streamline, the procedure is much the same. See sketch 11. The downstream extension of the streamline through F_3 results in a backwards-projected Mach cone shown here by a circle. The intersections of the base curve and lines F_2-F_3 and F_3-F_4 define base-point 1 and 3 respectively. The properties at each base point are also determined by interpolating between the appropriate pairs of data points. Base points 2 and 4 are determined as discussed in the preceding paragraph.



Sketch 11

Shock Point Solution

The shock point solution for this program is a radical departure from that discussed in Reference 5. After publication of Reference 5 it was found that the shock point procedure used there was unstable due to the use of the shock deflection angle as the principal variable ($\partial\beta_{\text{shock}}/\partial\eta$ is always greater than 1.0). Since θ and ψ define a local flow direction, (and hence the shock deflection angle at the shock wave) and also appear directly in the compatibility equations, in order to stabilize the solution any new shock point solution cannot use them directly.

The location of a new shock point is based upon the extension of the average "two dimensional shock line" from an existing shock point. See sketch 12.

Sketch 12

If \bar{N} is the normal to the shock wave, the direction of the two dimensional shock-line, \bar{S} , is defined by

In finite difference form, \bar{N} is the average of the shock normals at the upstream shock point and the present value at the new shock point.

$$\bar{N} = \bar{V}_2 - \bar{V}_3 \quad (30)$$

From the new point location the Mach conoid is projected back upstream, just as for body and field points, and base points located along S_3-S_2 , S_3-B_3 , S_3-S_4 . All properties at point 2 are determined by interpolation. At points 1 and 3 the local value of θ and ψ are determined by interpolation. From these the remaining properties determined from the Rankine Hugoniot relations. Since θ and ψ are known (by interpolation) and since

the value of η may be determined. Similarly, knowing M_∞ and η the appropriate shock wave angle, β_{shock} can be determined along with the pressure and Mach number behind the shock wave.

For a zeroth approximation to the properties at the new shock point the values at the preceding point are used. The new principal variables are now taken to be P_c and ψ_c . Since P_c , the pressure, effectively defines the shock wave angle, β_{shock} , the new process is stable ($\partial\eta/\partial\beta_{\text{shock}} < 1$). Using the value of P_c , the deflection angle across the shock wave, η , can be determined and knowing η and ψ_c , θ_c can be determined from Equation 31.

The compatibility relations, Equation (26), are now solved for the two unknowns,

$$\begin{bmatrix} \sum A_i (A_i + B_i \frac{\partial \theta}{\partial P}) & \sum C_i (A_i + B_i \frac{\partial \theta}{\partial P}) \\ \sum A_i (C_i + B_i \frac{\partial \theta}{\partial \psi}) & \sum C_i (C_i + B_i \frac{\partial \theta}{\partial \psi}) \end{bmatrix} \begin{bmatrix} P_c \\ \psi_c \end{bmatrix} = \begin{bmatrix} \sum D_i (A_i + B_i \frac{\partial \theta}{\partial P}) \\ \sum D_i (C_i + B_i \frac{\partial \theta}{\partial \psi}) \end{bmatrix} \quad (32)$$

The partial derivative $\frac{\partial \theta}{\partial \psi}$ is obtained from Equation (31). The value of $\frac{\partial \theta}{\partial P}$ is determined from $\frac{\partial \theta}{\partial \eta} \frac{\partial \eta}{\partial P}$. Equation 31 is used to determine $\frac{\partial \theta}{\partial \eta}$, and the oblique two-dimensional shock-wave equations for $\frac{\partial \eta}{\partial P}$.

Having determined P_c and ψ_c from Equation (32), the corresponding value of θ_c can be determined from Equation (31), since η is a function of pressure ratio across the shock.

These then are the new values of P_c , θ_c , and ψ_c for the next round in the shock wave calculations. The calculation sequence is continued until the changes in the values of the principal variables in successive iterations satisfy the following inequalities,

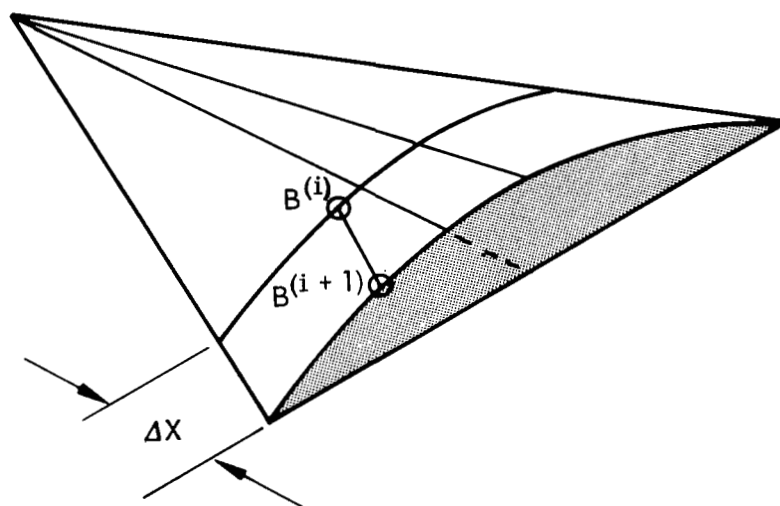
$$\begin{aligned} \left| \frac{P_c^{(i)} - P_c^{(i-1)}}{P_c^{(i)}} \right| &\leq 1 \times 10^{-6} \\ \left| \theta_c^{(i)} - \theta_c^{(i-1)} \right| &\leq 1 \times 10^{-5} \\ \left| \psi_c^{(i)} - \psi_c^{(i-1)} \right| &\leq 1 \times 10^{-5} \end{aligned}$$

or until the overall process exceeds 50 iterations. When the latter occurs, the program prints a diagnostic message and terminates the problem.

When the values for the new shock point are converged, the program calculates new averages for the Mach cones, and relocates the base points. The convergence process described above is carried out using these new base point values. This process continues until complete convergence of all properties at the new shock point is obtained.

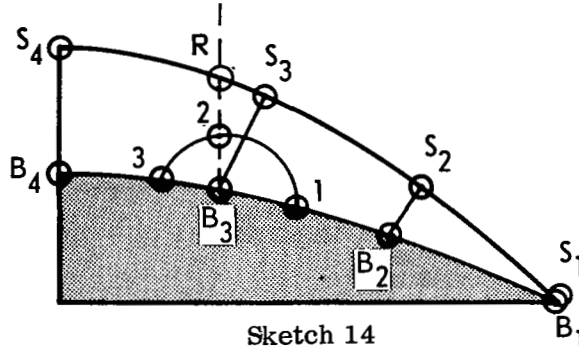
Body Point Solution

The determination of the location of new body points is carried out by extending the streamline from an existing base point, say $B^{(i)}$ in sketch 13, until it intersects the next $X = \text{constant}$ plane. This first approximation to the location of a new body point may or may not lie on the body. If it does not the point is moved to the body, and appropriate θ and ψ values defined. As the solution progresses, the directions of the streamline at points $B^{(i)}$ and $B^{(i+1)}$ are averaged and a new position determined so that upon convergence $B^{(i+1)}$ will lie on the streamline from point $B^{(i)}$.



Sketch 13

The Mach cone back projected from the new body point location traces a curve on the previous data surface as shown in Sketch 14. The location of the base points are determined by the intersection of this base curve and lines connecting points $B_3 - B_2$, $B_3 - B_4$ and a vertical line from B_3 to the shock wave point R. The properties at these points are determined by interpolation.



As before the three compatibility equations can be used to define a residual given by Equation (27). Along with this equation, the condition of flow tangency at the body surface must be satisfied;

$$\bar{N} \cdot \bar{S} = 0 = N_X \sin \theta_c \cos \psi_c + N_Y \cos \theta_c + N_Z \sin \theta_c \sin \psi_c \quad (33)$$

Here \bar{N} is the normal to the body, and \bar{S} the local streamline direction. By differentiating Equation (27) with respect to P_c and ψ_c , and noting that θ_c is now a function of ψ_c through Equation (33), the conditions for a minimum value of g are

$$P_c \sum A_i^2 + \psi_c \sum A_i C_i = \sum A_i D_i - \theta_c \sum A_i B_i \quad (34a)$$

$$P_c \sum A_i \left(C_i + B_i \frac{\partial \theta}{\partial \psi} \right) + \psi_c \sum C_i \left(C_i + B_i \frac{\partial \theta}{\partial \psi} \right) = \sum D_i \left(C_i + B_i \frac{\partial \theta}{\partial \psi} \right) - \theta_c \sum B_i \left(C_i + B_i \frac{\partial \theta}{\partial \psi} \right) \quad (34b)$$

Equations (33), (34a) and (34b) now form a set of three equations in three unknowns, P_c , θ_c and ψ_c . As a first approximation the value of ψ from the upstream body point is used. Equation (33) is then solved for θ_c ,

$$\tan \theta_c = \frac{-N_Y}{N_X \cos \psi_c + N_Z \sin \psi_c} \quad (35)$$

These values of θ_c and ψ_c are used with Equation (34a) to determine P_c . These values of P_c , θ_c , and ψ_c are then used in Equation (34b) which is solved by iteration for ψ_c . The process then continues with a determination of the next approximation to θ_c via Equation (35). The overall iterative process continues until no further significant change occurs in the values of P_c , θ_c and ψ_c . This is the inner loop of the body point process, for the location and properties at the base points have not yet been re-evaluated.

Using the values of θ_c , ψ_c and θ , ψ at the upstream body point, the location of the new body point is recalculated. New average properties for the Mach conoid passing through each base point are formed, and the location of properties at these base points re-determined.

This process continues until the increments between successive iterations become

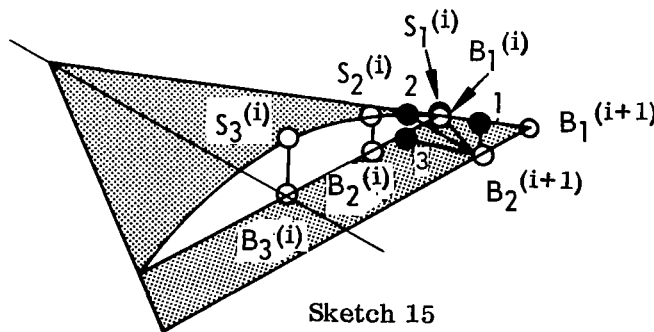
$$\left| \frac{P_c^{(i)} - P_c^{(i-1)}}{P_c^{(i)}} \right| \leq 1 \times 10^{-5}$$

$$\left| \psi_c^{(i)} - \psi_c^{(i-1)} \right| \leq 1 \times 10^{-5} \text{ radians}$$

$$\left| \theta_c^{(i)} - \theta_c^{(i-1)} \right| \leq 1 \times 10^{-5} \text{ radians}$$

Knowledge of the plane of symmetry is used to reduce the amount of calculations. For body points falling on the plane of symmetry the value of ψ is set to zero, and the properties of the base points on either side of the plane of symmetry are made proper "images" of each other.

A special case occurs with the second body point on a new surface. In the sketch below, the second base point on the new surface, $B_2^{(i+1)}$ lies on the streamline through the first body point on the previous surface $B_1^{(i)}$. For the first approximation the base points are determined as shown. Base point 1 lies on the leading edge of the wing. Base point 2 lies on the shock wave and base point 3 lies on the body. Due to the poor spacing of the bicharacteristics around the Mach conoid this solution will contain a moderate amount of error.



Sketch 15

By experimentation it was found that a much improved solution could be obtained if only the bicharacteristics to base points 1 and 3 were used in the compatibility relations. With two compatibility relations, and the tangency condition, the problem was completely determined. Also, as a test, this two-bicharacteristics type of solution was

used along the entire body, but the inboard solutions were less accurate than the standard three-bicharacteristics solution.

A similar problem occurs on the second shock point on each surface. The same type of cure, i. e., the use of two-bicharacteristics instead of three, was found to be effective here.

The Initial Value Surface

The two conflicting requirements for an Initial Value Surface are:

- (1) The data be easily generated
- (2) The data represent the final answer with sufficient accuracy to permit the 3DMoC method to reach convergence.

These two requirements have been successfully met on both the expansion and compression side.

The Compression Surface. The shape of the shock wave on the IVS on the compression side of the wing was taken to be

$$Y = Y_{\max} \left[1 - \left(\frac{Z}{Z_{\max}} \right)^n \right] \quad (36)$$

The maximum Y is determined from applying the tangent wedge rule to the centerline of the wing. The value of n is evaluated from

$$n = - \frac{\tan \sigma}{Y_{\max}/Z_{\max}} \quad (37)$$

where σ is the shock wave angle in the $X = \text{const}$ plane measured from the $Y = 0$ plane. Note that σ is always negative

The derivative, $\frac{\partial Y}{\partial Z}$, of Equation (36) is

$$\frac{dY}{dZ} = \tan \sigma \left(\frac{Z}{Z_{\max}} \right)^{n-1} \quad (38)$$

To determine the normal to the shock wave at any point on the IVS, the location vector, $P = X \bar{i} + Y \bar{j} + Z \bar{k}$, is crossed with the tangent vector of Equation (38). The non-normalized result is

$$\bar{N} = \left(\frac{Z}{X} \frac{dY}{dZ} - \frac{Y}{X} \right) \bar{i} + (1) \bar{j} - \left(\frac{dY}{dZ} \right) \bar{k} \quad (39)$$

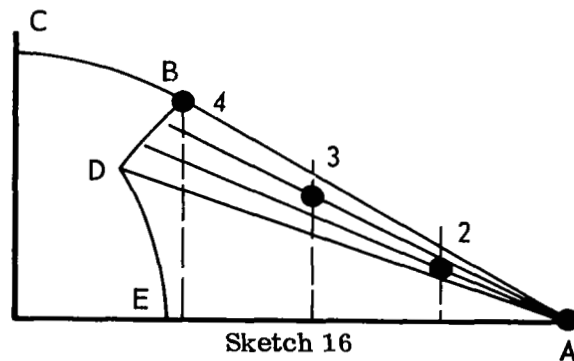
After normalization, $M_\infty (\bar{V}_\infty \cdot \bar{N})$ gives the Mach number normal to the shock, and thus defines all the properties just behind the shock wave.

Using the same ψ and P distribution on the body as on the shock, and evaluating the corresponding θ from the tangency condition provides the body point data on the IVS. At the body surface, on the IVS as in the 3DMoC calculations, the total pressure is taken to be constant at the leading edge value.

The number of points on the IVS is an input variable. Experience has shown that few points are needed when starting thin wings at small angles of attack. Broadly speaking, 9 points should be used for wings with curved cross sections at moderate to large angles of attack, but 3 points otherwise.

It is possible for Equation (36) to provide shock shapes with a pressure increase inboard of the leading edge. When this occurs, a reduction in the number of IVS points will "step over" this pressure rise and permit the calculations to start correctly.

The expansion surface: On the expansion surface a Prandtl-Meyer fan is generated at the leading edge. As shown in Sketch 16, the fan originates at the leading edge, point A, and spreads inboard to fill the region between B and D. The line B-D represents the locus of the points of tangency of the envelope lines from point A to the various intermediate expansion Mach cones. Point B, for instance, is the undisturbed free stream Mach cone tangency point and D the fully expanded cone point. The expansion fan is defined in terms of N ray lines representing equal increments in the expansion process. The distance from A to B is then divided into $N-1$ equal intervals. The tangency point on the undisturbed-stream ray line is used to define the location of and properties at point 4. The second ray line and the second outboard line define point 3, etc., until the last point is located at the leading edge.



Points 1 to 4 (the number is arbitrary between 4 and 50) now represent the continuous expansion process. An orthogonal polynomial curve fit (References 11, 12) is then used to accurately represent Y, P, θ, ψ as a function of Z/Z_{\max} , the spanwise coordinate. From point B to C the curve is a portion of the ellipse defining the free stream Mach cone from the apex of the wing. Thus, the curve defined by 1-2-3-4-C is the expansion surface IVS. In addition, this surface is the prescribed boundary surface for each downstream station. Thus, there is no "shock-line" calculation for the expansion surface. The IVS boundary curve is merely expanded to fit the local span, and the necessary body and field points calculated.

Leading Edge Conditions

Swept Wedge

There are two components to the shock deflection angle across a swept wedge; one due to the sweep of a flat plate at angle of attack and the second due to the slope of a body with finite thickness at the leading edge.

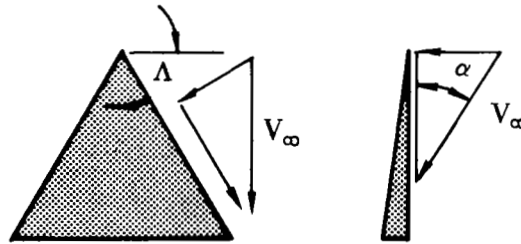
From Sketch 17 it is obvious that the Mach number and angle of attack normal to the leading edge are given by

$$M_{\infty n} = M_{\infty} \sqrt{1 - \cos^2 \alpha \sin^2 \Lambda} \quad (40)$$

$$\alpha_n = \arcsin \left(\frac{\sin \alpha}{\sqrt{1 - \cos^2 \alpha \sin^2 \Lambda}} \right) \quad (41)$$

$$\eta = \alpha_n + \eta_T \quad (42)$$

where η_T is the thickness angle normal to the leading edge



Sketch 17

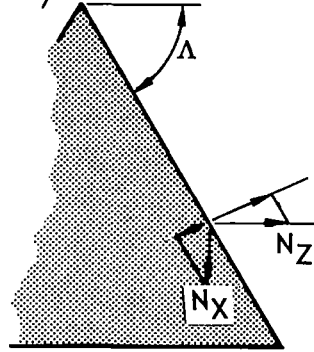
From η and $M_{\infty n}$, the shock wave angle, β_n , normal to the leading edge can be determined, and all other properties behind the shock wave evaluated.

If the body surface normal has components, N_X , N_Y , N_Z in the X, Y, Z direction respectively, the thickness contribution can be easily determined. Sketch 18 shows a plan view of the wing. The X and Z components of the body surface normal can be combined to determine the normal to the leading edge in the $Y = 0$ plane

$$n_1 = N_Z \sin \Lambda - N_X \cos \Lambda \quad (43)$$

The thickness contribution is then

$$\eta_T = \arctan\left(\frac{n_1}{N_Y}\right) = \arctan\left[\frac{N_Z \sin \Lambda - N_X \cos \Lambda}{N_Y}\right] \quad (44)$$



Sketch 18

Swept Prandtl-Meyer Corner

Equations (40) to (44) apply equally well to swept expansion corners if the angle of attack is taken to be negative. Thus, the resultant expansion angle normal to the leading edge given by Equation (42) should be a negative quantity.

The compatibility equations for rotationally-symmetric flow are given in Reference 5 by Equation (65). By setting the incremental length along the characteristics to zero we have the governing equation for Prandtl-Meyer expansions:

$$\frac{1}{\gamma} d \ln P - \frac{d \eta}{\sin \mu \cos \mu} = 0 \quad (45)$$

or in finite difference form

$$\ln P_2 = \ln P_1 + 2\gamma \frac{\eta_2 - \eta_1}{\sin(\mu_1 + \mu_2)} \quad (46)$$

Thus, given an incremental expansion $(\eta_2 - \eta_1)$, the pressure corresponding to η_2 can be determined in an iterative process, since μ_2 is a function only of P_2 .

The process used in this program initially divides the total expansion increment, η from Equation (42), into 4 equal increments, and calculates the final pressure, P_4 , by using Equation (46) sequentially to determine P_2 from P_1 , P_3 from P_2 , and P_4 from P_3 . The total increment η , is now divided by 5, and the final pressure, P_5 determined. If the difference in pressure is not sufficiently small, the total increment is divided into 6 steps. This process is continued until a sufficiently small $[P_m - P_{m-1}]$ is determined using m equal increments to expand through the entire expansion angle given by Equation (41).

The solution to the swept expansion corner is started using a pressure $P_1^* = P/P_{t\infty}$ corresponding to the Mach number normal to the leading edge,

$$P_1^* = \left[1 + \frac{\gamma-1}{2} (M_{\infty n})^2 \right]^{-\frac{\gamma}{\gamma-1}} \quad (47)$$

The array of pressures obtained during the solution, P_1^* , P_2^* , ..., P_m^* are then relative (rather than absolute) pressures. By multiplying each by $\frac{P_\infty/P_{t\infty}}{P_1^*}$ the local value of $P_1/P_{t\infty}$ is obtained, and hence the total local Mach number can be determined.

The free-stream velocity component parallel to the leading edge is

$$\frac{V_{\infty p}}{V_{\max}} = \frac{V_\infty}{V_{\max}} \cos \alpha \sin \Lambda \quad (48)$$

$$\frac{V_i}{V_{\max}} = \sqrt{\frac{\frac{\gamma-1}{2} M_i^2}{1 + \frac{\gamma-1}{2} M_i^2}} \quad (49)$$

Hence the normal component is

$$\frac{V_{i,n}}{V_{\max}} = \sqrt{\left(\frac{V_i}{V_{\max}}\right)^2 - \left(\frac{V_{\infty p}}{V_{\max}}\right)^2} \quad (50)$$

The local flow direction is completely defined by the normal and parallel components, equations (48) and (50).

Thus, the swept expansion corner is completely defined.

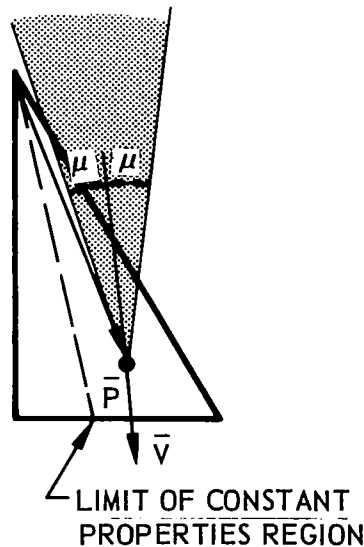
Constant-Property Regions

During the early development work on this program no attempt was made to set properties in the constant-property region near the leading edges on flat-plate or modified-wedge wings. When the results showed that the program was providing stable, accurate results in this region, with only a small rounding off of the "corner" between the constant-pressure outer region and the varying-pressure center region, it was decided to set properties in these outer regions. By this means the computing time required for the overall solution would be reduced to a minimum.

The test for the location of a point is shown in sketch 19. At a given point where the local velocity vector is \bar{V} , and \bar{P} is the location vector from the apex of the wing, if

$$\frac{\bar{P} \cdot \bar{V}}{|\bar{P}| |\bar{V}|} \leq \cos \mu \quad (51)$$

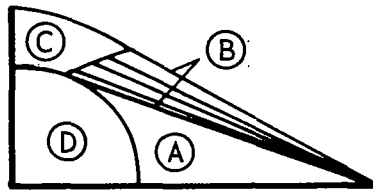
the point lies in a constant property region and the properties can be assigned rather than calculated.



Sketch 19

A special case occurs for modified-wedge wings. If Z^* , the point of tangency between the wedge and the center region, lies outboard of the constant property Mach cone, the program assumes only that properties from Z^* outboard are constant. This ignores a small curvilinear region above and inboard of Z^* which could be set but the additional computing load is so small that the additional logic to accomplish this was not worth the cost.

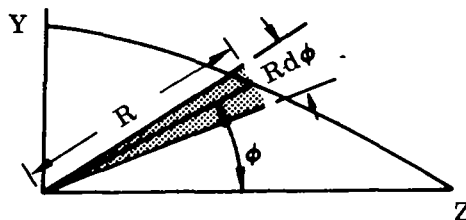
On the expansion-side solution, a more elaborate test of location is necessary. As seen in sketch 20 the test given by Equation (51) will identify points inside or outside of region D. If a point lies outside of region D its angular location with respect to the leading edge must be checked. If its position angle is less than the last rayline of the Prandtl-Meyer fan, the point then lies in region A where the constant leading edge properties may be assigned (unless the wing is a general conic -- in which case the whole of region A must be calculated). If its location angle with respect to the leading edge is greater than the last rayline angle, the point lies either in region B or C. By checking the radial distance from the leading edge the location can be established. If the point lies in region C no properties can be assigned; a complete calculation must be carried out. If the point lies in region B the properties must be evaluated by means of the curve fits to the Prandtl-Meyer data.



Sketch 20

When the calculations have been carried downstream far enough to satisfy the convergence criteria, the contributions of the surface pressures to the normal force, axial force, lift, and drag coefficients of the total wing are calculated.

The axial force is determined from the pressure and thickness distribution by integrating in polar coordinates, as shown in sketch 21.



Sketch 21

$$\frac{\text{X-FORCE}}{Q} = 2 \int_0^{\pi/2} C_P \frac{R^2}{2} d\phi \quad (52)$$

where

$$R^2 = Y^2 + Z^2$$

To convert to the axial force coefficient, C_X , Equation (52) is divided by the reference area, which for wings is the plan form area.

Since for a delta wing with sweep back angle Λ , the wing area is

$$A = \frac{b^2}{2} \tan \Lambda \quad (53)$$

$$C_X = \frac{\text{X-FORCE}}{QA} = \frac{2}{b^2 \tan \Lambda} \int_0^{\pi/2} C_P R^2 d\phi = \frac{2}{\tan \Lambda} \int_0^{\pi/2} C_P \left(\frac{R}{b}\right)^2 d\phi \quad (54)$$

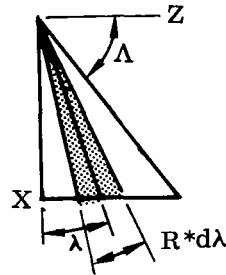
Similarly for the normal force coefficient,

$$C_N = \frac{2}{\tan \Lambda} \int_0^{(\pi/2 - \Lambda)} C_P \left(\frac{R^*}{b}\right)^2 d\lambda \quad (55)$$

where

$$R^* = X^2 + Z^2$$

and the angle λ is defined in sketch 22.



Sketch 22

For lift and drag coefficients, the well-known conversions are used

$$C_L = C_N \cos \alpha - C_X \sin \alpha \quad (56)$$

$$C_D = C_N \sin \alpha + C_X \cos \alpha \quad (57)$$

Since the flow has been assumed to be conical, the moment arm of the normal force is at the center of area. The pitching moment about the apex, referred to the length of the wing root chord is then

$$C_{M_{APEX}} \approx -\frac{2}{3} C_N \quad (58)$$

Equation (58) neglects a component due to thickness which will be small for the cases capable of being analyzed here.

RESULTS

During development of the previously-discussed program a number of different cases were calculated, and comparisons made between the results and both experimental data and other theoretical work. Since the primary objective was the development of an accurate, reliable computerized method, primary emphasis was given to those cases which gave rise to problems in the numerical solution. A selection of results and comparisons follows, and for the reason given above should not be considered an exhaustive comparison of inviscid theory with experimental data.

A primary problem in the use of any three-dimensional method is that of visualizing the results. In order to facilitate the analysis of results, the 3DMoC program was provided with an option for punching the properties of each calculated data point on cards. A cathode ray tube plotter program was then built to read these data and plot the results in meaningful form.

Figures 1 to 13 show examples of these electronically-plotted graphs for the compression surface calculation of the flow over a wedge cross-section wing with a 50° sweep angle, a \hat{Z}^* of 0.27 and a 5° wedge normal to the centerline. This case is for $M_\infty = 6.0$ and $\alpha = 10^\circ$. The data points have been connected with straight lines for clarity.

Figure 1 shows the body surface streamlines. The three-point IVS is at the left. Each new surface has a new streamline added at the leading edge. The streamlines all move outboard in this physical case. However, in the conical sense, all streamlines are

moving inboard. This can be clearly seen by laying a straightedge across the wing and locating it to pass through the wing apex.

Figure 2 shows the pressure coefficient distribution along each body streamline, shown in Figure 1. The initial pressure value on each streamline is set by the IVS. The lowest line corresponds to the centerline streamline. This pressure rather quickly reaches its asymptotic level, indicating convergence. All other streamline values continuously decrease, and approach the centerline value. This is due to the fact that the streamlines are moving inboard in the conical sense as previously discussed. Note that such added streamlines pass through a constant property region before entering the central zone of influence.

Figures 3 and 4 show the variation of θ and ψ along the body surface streamlines. A smooth variation to the converged values is seen.

Figures 5, 6, and 7 are the variations of C_p , θ , ψ along the two-dimensional shock lines (refer to the Shock Point section for the description of these shock lines). Again a smooth variation is seen. Figure 8 shows the total-pressure variation along the two-dimensional shock lines.

Figure 9 shows the final converged geometry of the shock, body, and field points. Notice the straight outer region of the shock wave, and the very flat central region.

The converged spanwise distribution of C_p for body, shock, and field lines is given in Figure 10. Here the constant-property outer region is clearly seen. The constant-property region extends farther inboard on the shock wave than on the body.

The spanwise distribution of θ is given in Figure 11. Inboard of the constant-property region the θ values vary smoothly to their centerline value.

Figure 12 shows the spanwise variation of ψ . The very small variation in the magnitude of ψ should be noted.

Figure 13 shows the spanwise variation of total pressure.

Through the use of detailed plots such as these the quality of the solutions can be easily assessed. Without such detailed checks evaluation of solutions is tedious and time consuming.

Compression Surface

FLAT PLATE: Figure 14 compares the spanwise pressure distribution for a flat plate with $\Lambda = 45^\circ$ at $M_\infty = 3.0$ and $\alpha = 4^\circ$ with the results of Fowell (Reference 1)

and linearized theory. Fowell used a relaxation method of calculation and a value of 1.405 for the ratio of the specific heats. These differences cause the minor disagreements between the results from the two methods. There is a considerable difference between the results of the two "exact" solutions and those of linear theory, both in level and width of the central region of influence. This, of course, is neither unknown nor unexpected.

Figure 15 is a plot of the spanwise pressure distribution on a 70° swept flat plate at $\alpha = 5^\circ$ and 10° in helium ($\gamma = 5/3$), as compared with experimental data from Reference 13. For the lower angle of attack experimental data all lie above the theoretical data. This is due to the effects of viscid-inviscid interaction. At the larger angle of attack the experimental data now lie above and below the theoretical inviscid data. This is to be expected in these cases where viscid-inviscid interaction is weaker.

Figure 16 shows the variation of centerline and leading-edge pressures with angle of attack for a 50° swept flat delta wing at a Mach number of 10.0. The present method was used to determine the properties at angles of attack up to 30° . Note that shock detachment occurs at an angle of attack of 31.5° . The pressure variation according to linear theory is also given in this plot. Above 8° angle of attack linear theory and the exact calculation diverge rapidly, as expected.

Two techniques are used at times to approximate the centerline pressure on flat plate wings: the tangent wedge and the tangent cone approximations. (The leading edge, of course, corresponds exactly to swept wedge data). Results from these two techniques are also plotted in Figure 16. The tangent wedge approximation yields pressures higher than the centerline values, and almost the same as the leading edge pressures. The tangent cone approximation on the other hand yields pressures too low.

Figure 17 compares the pressure distribution on a 50° swept flat plate at $\alpha = 14^\circ$ and $M = 5.08$ as generated by two methods with data from Reference 14. The results from Reference 3 were obtained by scaling from very small scale graphs; therefore some error is possible. The results of the present method compare favorably with those of Reference 3, and both are somewhat lower than the experimental data.

Some difficulties with flat plate solutions were encountered when running cases at angles of attack very close to the shock-detachment angle of attack. In one case ($M_\infty = 4$, $\Lambda = 50$), a solution at $\alpha = 22.2^\circ$ (with $\alpha_{\text{detachment}} = 22.5^\circ$) failed due to problems encountered near the leading edge. Solutions were easily obtained at lower angles of attack, however. Figure 16, for example, shows data where the calculations were carried to within 1.5° of the detachment angle of attack.

Wedges: A complete analysis of the flow around a wedge shape wing was given in Figures 1-13 for a $Z^*/b = 0.27$. A second case, with a somewhat smaller radius for the center part ($Z^*/b = 0.04$) was run and the results are shown in Figures 18 and 19. Figure 18 shows the differences in the spanwise pressure distribution on the shock and the body. For the smaller center radius the pressure decrease is due only to the central region of influence. For the larger center radius case the pressure decrease is initially due to the change in body shape, compounded closer to the centerline by the central region of influence. Figure 19 shows the corresponding body and shock wave shapes.

General Conic: Flat plate and wedge type solutions were achieved without any unusual problems. However, general conic surfaces caused considerable trouble and their solution can be considered only a qualified success. In these cases the solution is conditionally stable, i.e., the solution tends toward the correct solution, but if run far enough will eventually diverge. This is analogous to the inverse-type blunt-body solutions where correct results can be obtained only by finding the right combination of step sizes. The present method, using a constant step size, represents a continuously decreasing step size in conical space.

As discussed in the Method Section, the program fixes values of the constant-property regions. On general conic sections there is no constant-property region. Hence the solution, including field points, must be carried out to the very leading edge. It was found that on the general conic wing the finite length of the first field line above the body introduced disturbances into the body point solutions. As the overall solution approached convergence, the perturbations increased in magnitude. Strangely enough, the shock point solutions were basically unaffected. On the wedge and flat plate wings, the outer edge of this finite-length field point line soon penetrates the constant-property region and is therefore effectively removed from influencing the solution.

The cross-flow Mach numbers in the circular-arc wing solutions were checked and it was found that the region of maximum perturbation was located in the transonic cross-flow region. This was interpreted to mean that the subsonic cross-flow data points were influencing the supersonic cross-flow data points through interpolation for these point properties. A test was built into the program to detect the case of supersonic cross flow at the new point, supersonic cross flow at the streamline data point, and subsonic cross flow at the inboard data point (note that the streamline data point and the inboard data point are on the upstream surface). For this special case only, the

bicharacteristic intersecting the line between the streamline and inboard data points was then dropped from the solution. This, and removal of field points, provided the circular-arc wing solution shown in Figure 20.

A similar case, starting from the same IVS but without the cross-flow Mach number check was run. These results showed a slight improvement over the results shown in Figure 20. This experiment shows that in the spatially asymptotic approach no special treatment is required in the transonic cross-flow region, and that the present 3DMoC solution is correctly posed.

A further series of runs for the same case, but using different maximum shock wave heights on the IVS, showed that a stable solution requires the IVS shock height to be somewhat higher than the converged results. When the IVS shock height is lower than the converged results, the 3DMoC solution soon generates bulges in the shock wave shape and becomes unstable.

Figure 20 shows the spanwise distribution of pressure on the body and behind the shock wave for a circular arc wing at $M_\infty = 8.1$ and $\alpha = 10^\circ$ ($\Lambda = 50^\circ$). Results obtained by the method of lines (Reference 4) are given for comparison. Good agreement is seen inboard to a Z/Z_{\max} of about 0.3. Inboard of this the present results are somewhat lower than those of Reference 4. Experimental data from Reference 14 are also plotted, and although viscous-inviscid interactions effects are present, particularly near the leading edge ($Z/Z_{\max} = 1.0$), the agreement with the inviscid calculations is good.

Figure 21 shows the corresponding shock wave shapes; very good agreement is seen between these results and those from Reference 4.

Expansion Side

Very few theoretical or experimental data were found for the expansion surface, at those angles of attack where viscous forces were not dominant.

Figure 22 shows the spanwise pressure distribution for a 50° flat plate delta wing at Mach 3 for an angle of 4° as determined by the 3DMoC method, by Reference 1, and by linear theory (all results are cross-flow shock-free). Good agreement is shown between those from Reference 1 and the one discussed here.

Figure 23 shows the pressure distribution variation over the 50° swept flat plate at a Mach number of 3.0 with angle of attack. As the angle of attack increases, the central region narrows and the pressure values in general become more negative.

The pressure gradient at the boundary of the central zone of influence increases with angle of attack, which may be indicative of the need for a cross-flow shock wave.

Figure 24 is an electronically generated plot of the final field and body shape. Compare the extent of the field on the expansion surface with that of the compression surface shown in Figure 9. The variations in the levels of the various field points are due to the fact that the field points are added at different times (whenever sufficient room exists) and that they are added at the midpoint of the available space. These causes, and the natural drift of the streamlines, leads to the unusual shapes shown in Figure 24.

Figure 25 shows the geometry of the expansion side flow field over a circular arc wing at $M_\infty = 8.1$ and 15° angle of attack. As in the flat plate case, the outer boundary is the fitted Prandtl-Meyer fan and Mach cone. The field point levels also vary here, for the same reasons discussed above.

The corresponding spanwise pressure distributions are given in Figure 26, showing a rapid drop on the body surface, coupled with a recompression near the centerline. This may be indicative of the need for a cross flow shock wave. Since the method used here does not calculate continuously along characteristic surfaces, the recompression waves which generate the coalescing Mach waves may not be detected.

Figure 27 shows, superimposed on one graph, all the body surface pressures from the IVS through the final surface. The IVS is the three point constant pressure line. A rapid pressure drop with distance downstream number along the centerline, is seen along with very early convergence to the correct properties near the leading edge. From a study of the envelope formed by the data it is obvious that the converged solution has been obtained.

CONCLUDING REMARKS

The use of the Three Dimensional Method of Characteristics in a spatial asymptotic approach to the solution of conical flow problems has provided good results for most cases and fair results for others, as shown in the RESULTS section. However, some additional remarks are in order. This type of solution appear to be "conditionally stable" in that any solution, if run far enough downstream will eventually become unstable. This behavior is reminiscent of the inverse blunt body solution where the process is unstable, but with an appropriate set of step sizes good engineering data can be obtained. This spatially asymptotic solution using a constant ΔX step size,

actually constitutes a constantly reducing step size when considered in a conical sense. However, the use of constant "conical" step sizes have showed no improvement.

For those wings with fairly large regions of constant properties at the leading edges (flat plates and wedges) the solutions are far more stable than those solutions requiring calculations right up to the leading edge. Indeed, the expansion surface, where the entire outer boundary is prescribed at every body station, is the most stable solution of all. Mathematically there is no difference between these problems; they are all hyperbolic in three dimensions, but elliptic/hyperbolic in two dimensions.

In summary,

1. Good compression surface solutions can be obtained for any flow field with a reasonably large constant-property outer region.
2. Without the constant-property outer region the solutions appear to be conditionally stable, in a manner similar to the inverse type of blunt body problem.
3. Good expansion surface solutions can be obtained, even without including cross flow shocks.*
4. As the radial gradients die out in this type of solution, the cross-flow gradients become more important, and the whole solution begins to behave more like an elliptic problem (even though a hyperbolic solution such as the 3DMoC was used).

Northrop Corporation, Aircraft Division

Hawthorne, California, March 14, 1970

* A good solution implies a solution to the inviscid flow field. The next question, and one not considered here, is how well inviscid expansion surface solutions correspond to reality.

REFERENCES

1. Fowell, L.R.: Exact and Approximate Solutions for the Supersonic Delta Wing. *J. Aero. Sc.*, vol. 23, no. 8, 1956, p. 709.
2. Babaev, D.A.: Numerical Solution of the Problem of Supersonic Flow Past the Lower Surface of a Delta Wing. *AIAA J.*, vol. 1, no. 9, Sept. 1963. p. 2224.
3. Voskresenskii, G.P.: Chislennye Reshenie Zadachi Obtekaniya Proizvol'voi Poverkhnosti Treugol'nogo Krila V Oblasti Czhatizy Cverkhzvykovim Potokom Gaza. (The Numerical Solution of the Problem of the Supersonic Flow of a Gas Around the Compression Side of a Triangular Wing of Arbitrary Surface) *Izv AN SSSR, MEKH Zhid i Gaza*, no. 4, 1968, p. 136.
4. South, J.C. jr; and Klunker, E.B.: Methods for Calculating Nonlinear Conical Flows, Presented at the NASA Symposium on Analytical Methods in Aircraft Aerodynamics, Oct. 28-30, 1969, Ames Research Center, Moffett Field, California.
5. Powers, S.A.; et al: A Numerical Procedure for Determining the Combined Viscid-Inviscid Flow Fields Over Generalized Three-Dimensional Bodies. Vol 1, Discussion of Methods and Results, and Instructions for Use of Computer Program. *AFFDL-TR-67-124*, vol. 1, Dec. 1967.
6. Chu, C.W.; and Ziegler, H.: Calculation of Multiple Rocket Engine Exhaust Planes by the Method of Characteristics, NOR 69-71, Northrop Corporation, 1969.
7. Chuskin, P.T.; Numerical Method of Characteristics for Three-Dimensional Supersonic Flows, *Progress in the Aeronautical Sciences*, vol. 9, Pergamon Press, 1969.
8. Chu, C.W.; et al: Interaction of Two Cylindrical Jets. *AIAA J.* vol. 5, 1967, pp. 375-376.
9. Chu, C.W.; Compatibility Relations and a Generalized Finite-Difference Approximation for Three-Dimensional Steady Supersonic Flow. *AIAA J.*, vol. 5, 1967, p. 493.

10. Butler, D.S.: The Numerical Solution of Hyperbolic System of Partial Differential Equations in Three Independent Variables, Proc. Royal Soc., A, vol. 225, pp. 232-252, 1960.
11. Abramowitz, M.; and Stegun, I.A. (Ed.): Handbook of Mathematical Functions. NBS Applied Mathematics Series, vol. 55, June 1964, p. 790.
12. Smith F.J.: An Algorithm for Summary Orthogonal Polynominal Series and Their Derivatives with Applications Curve-Fitting and Interpolation. Mathematics of Computation, April, 1965.
13. Barber, E.A.: Some Experiments on Delta in Hypersonic Flow, AIAA J, vol. 4, no. 1, January 1966.
14. Mead, H.R.; and Koch, F.: Theoretical Prediction of Pressures in Hypersonic Flow with Special Reference to Configurations Having Attached Leading-Edge Shock: Part II - Experimental Pressure Measurements at Mach 5 and 8. ASD Technical Report TR 61-60, May 1962.
15. Rakich, John V.; and Cleary, Joseph W.: Theoretical and Experimental Study of Supersonic Steady Flow Around Inclined Bodies of Revolution, AIAA Paper No. 69-187, presented at the 7th Aerospace Meeting, New York, January 20-22, 1969.

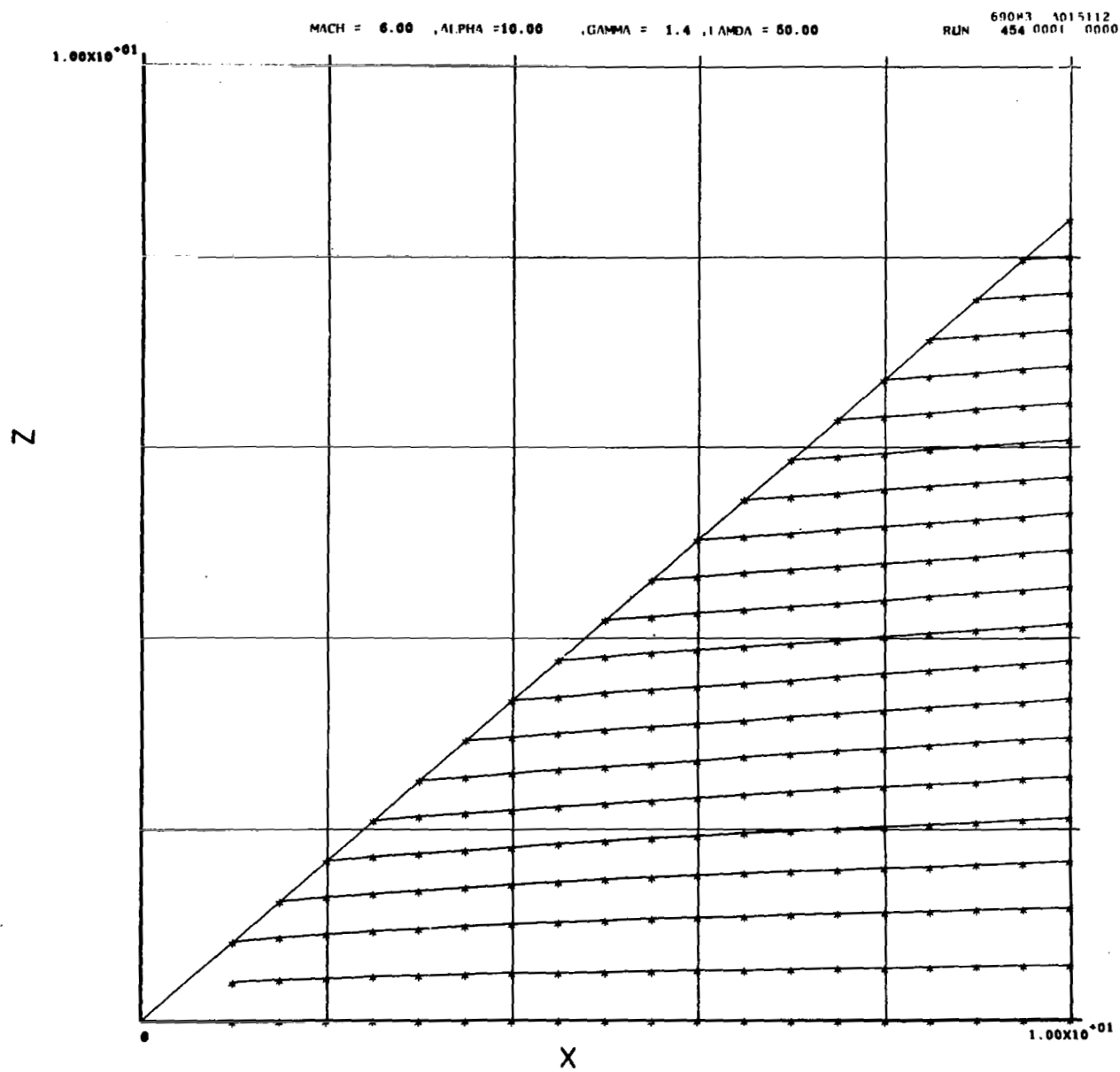


FIGURE 1. BODY SURFACE STREAMLINES

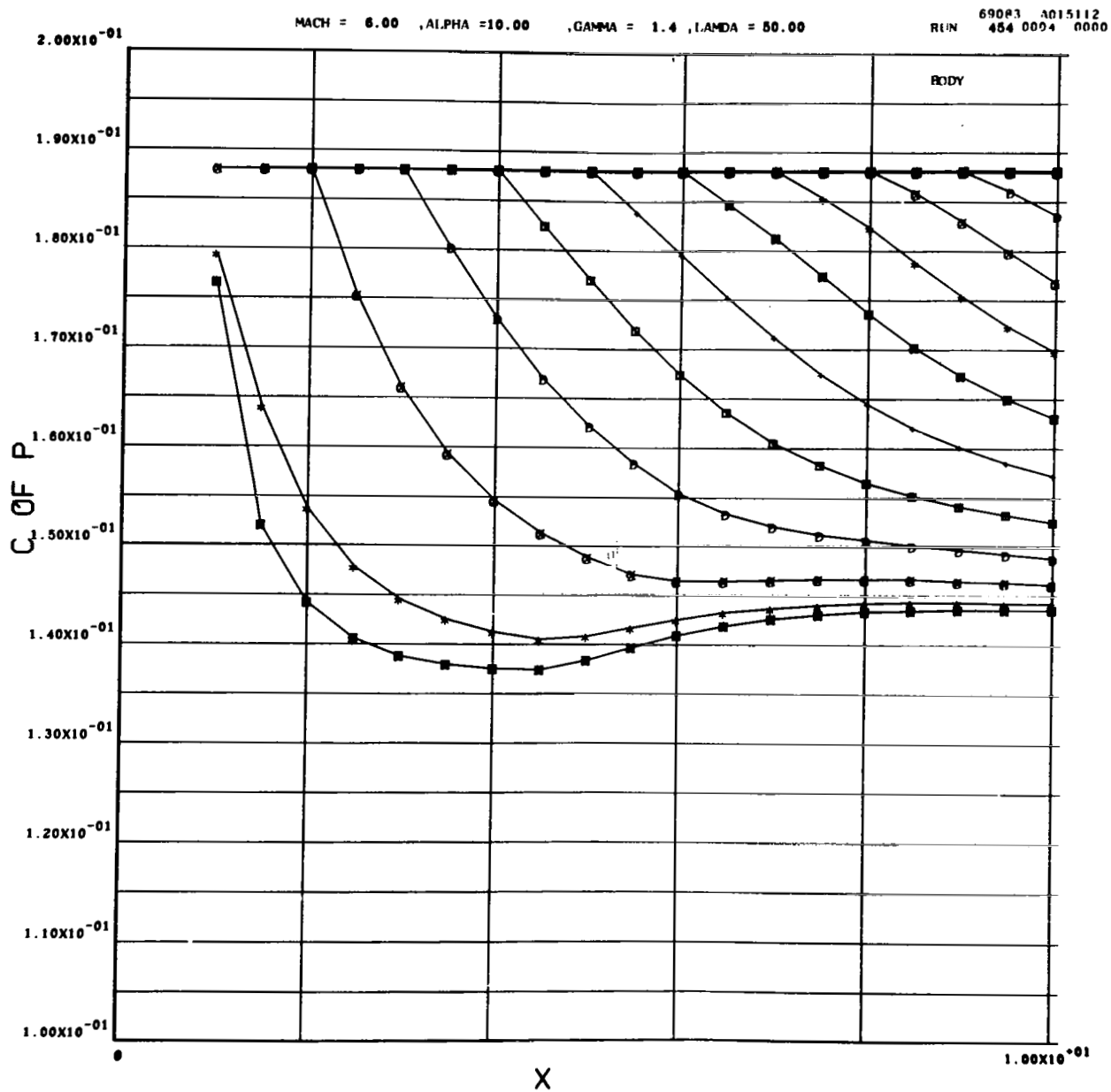


FIGURE 2. BODY SURFACE PRESSURE DISTRIBUTION ALONG STREAMLINES

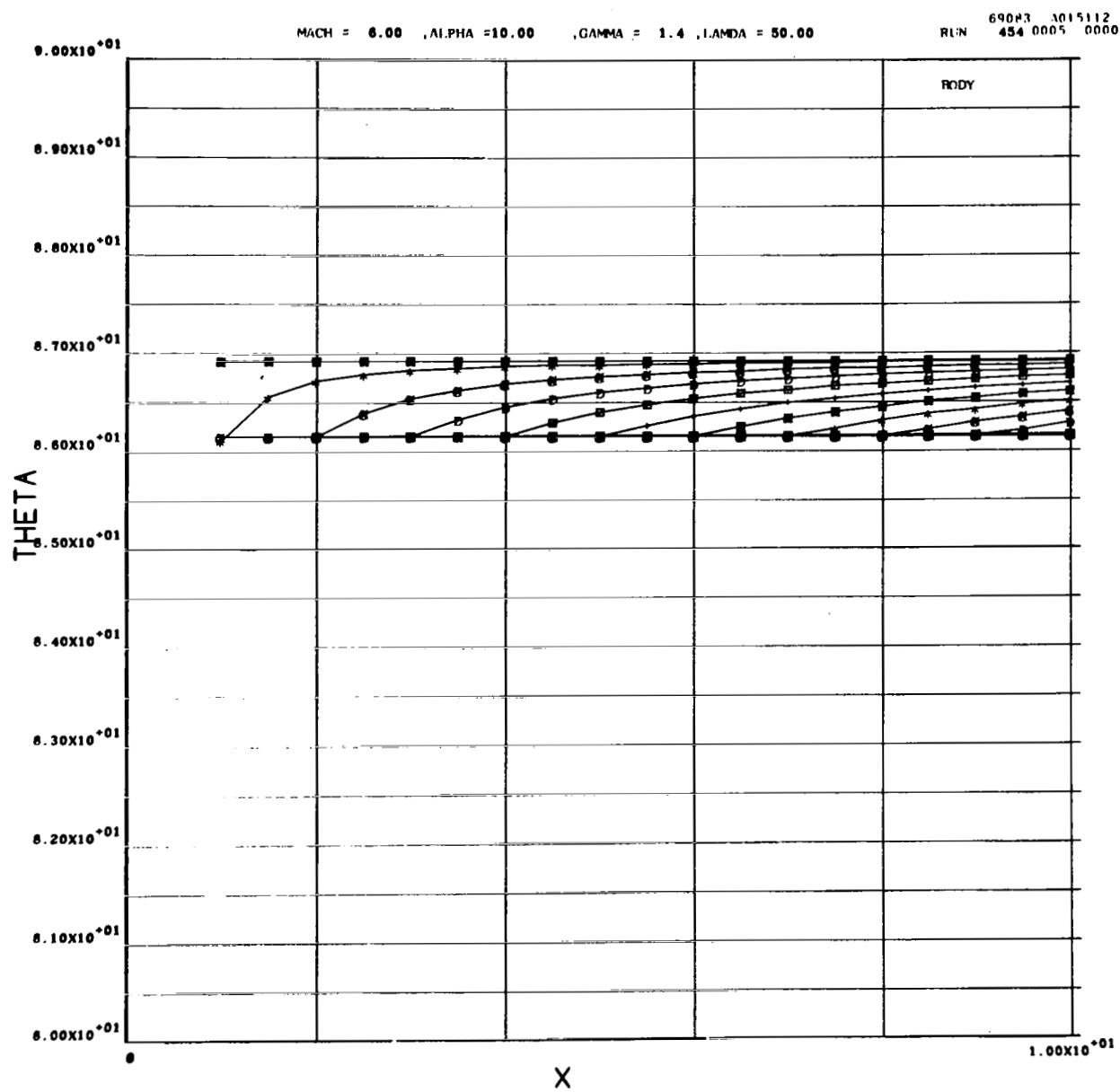


FIGURE 3. BODY SURFACE θ DISTRIBUTION ALONG STREAMLINES

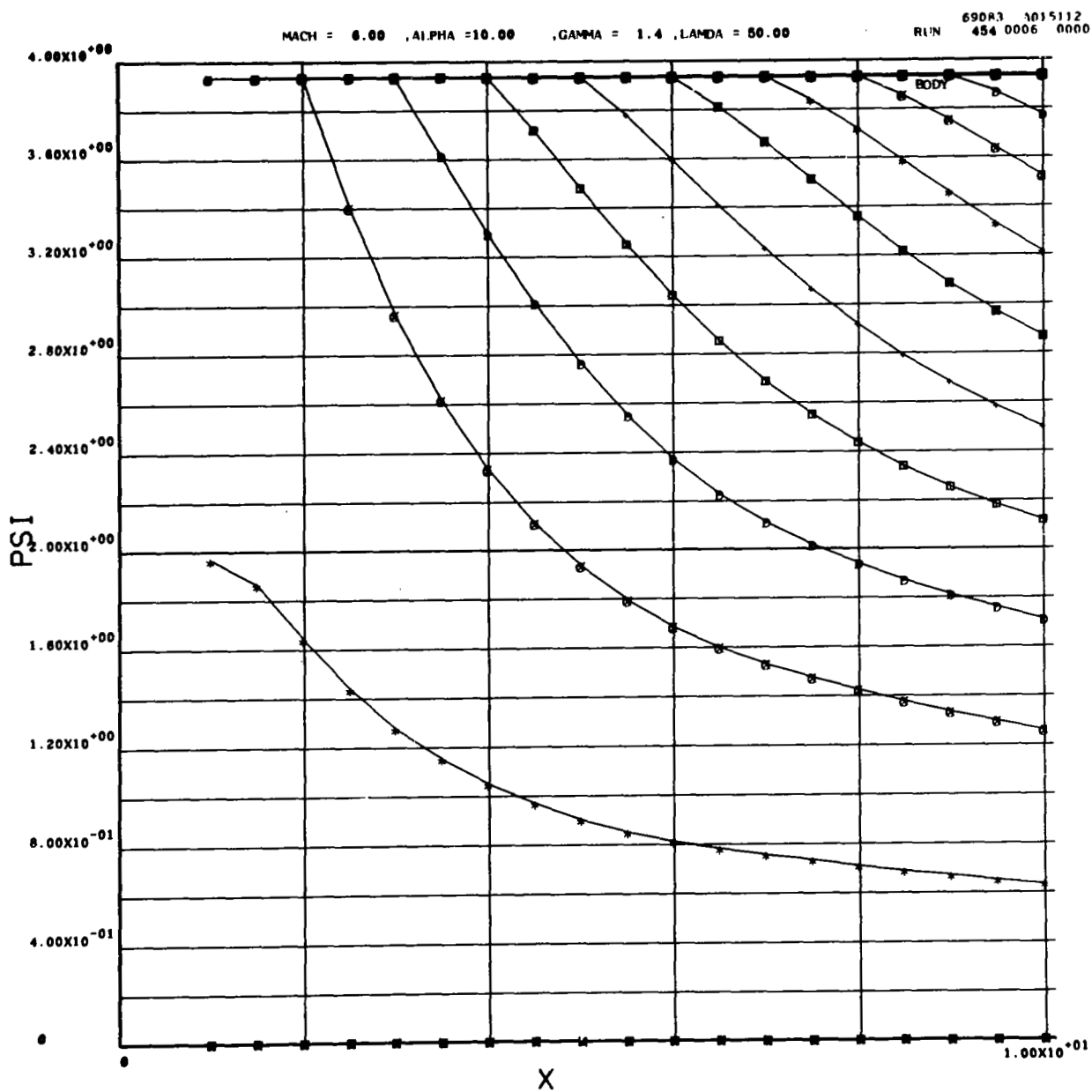


FIGURE 4. BODY SURFACE ψ DISTRIBUTION ALONG STREAMLINES

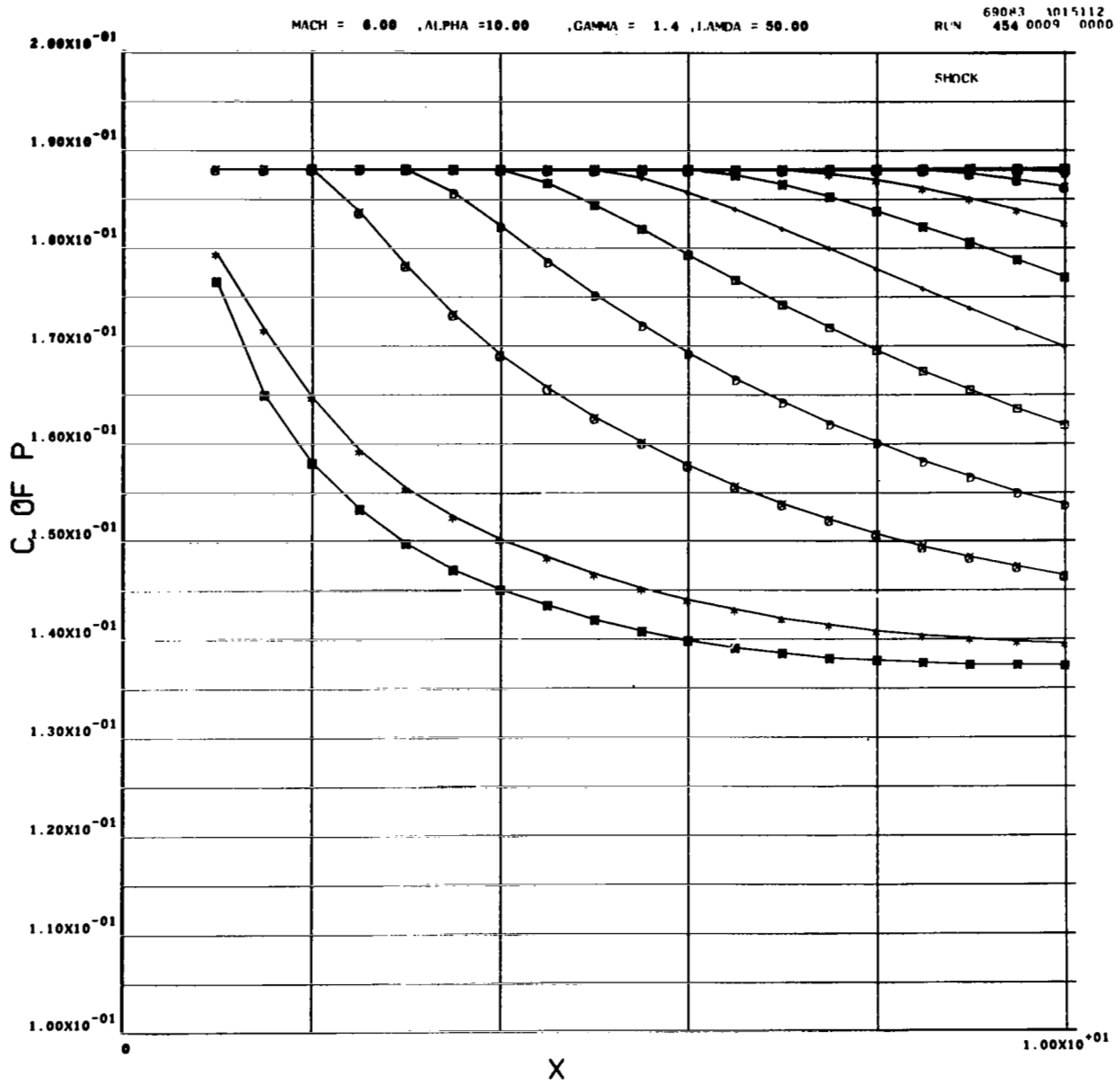


FIGURE 5. SHOCK WAVE PRESSURE DISTRIBUTION

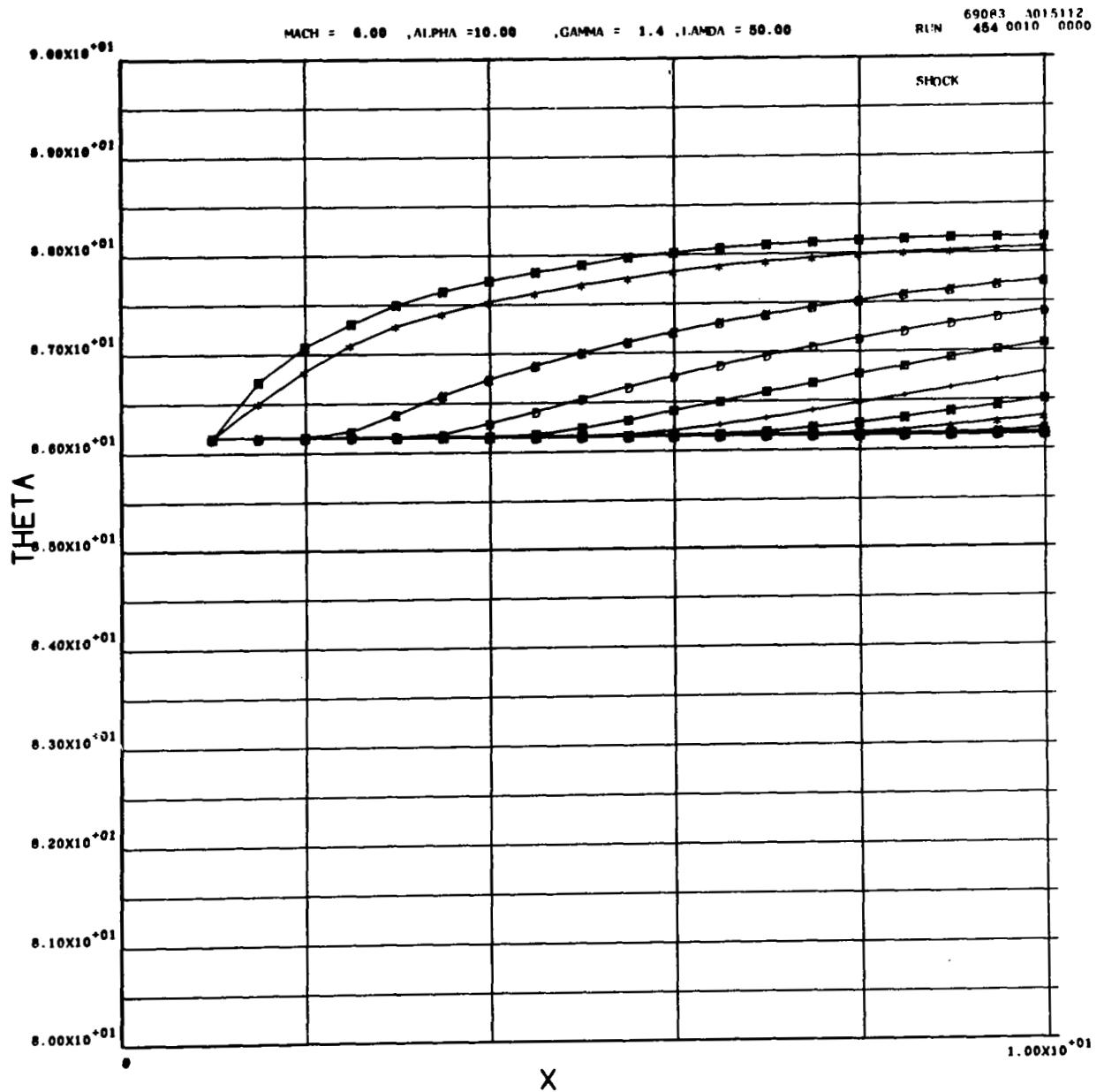


FIGURE 6. SHOCK WAVE θ DISTRIBUTION

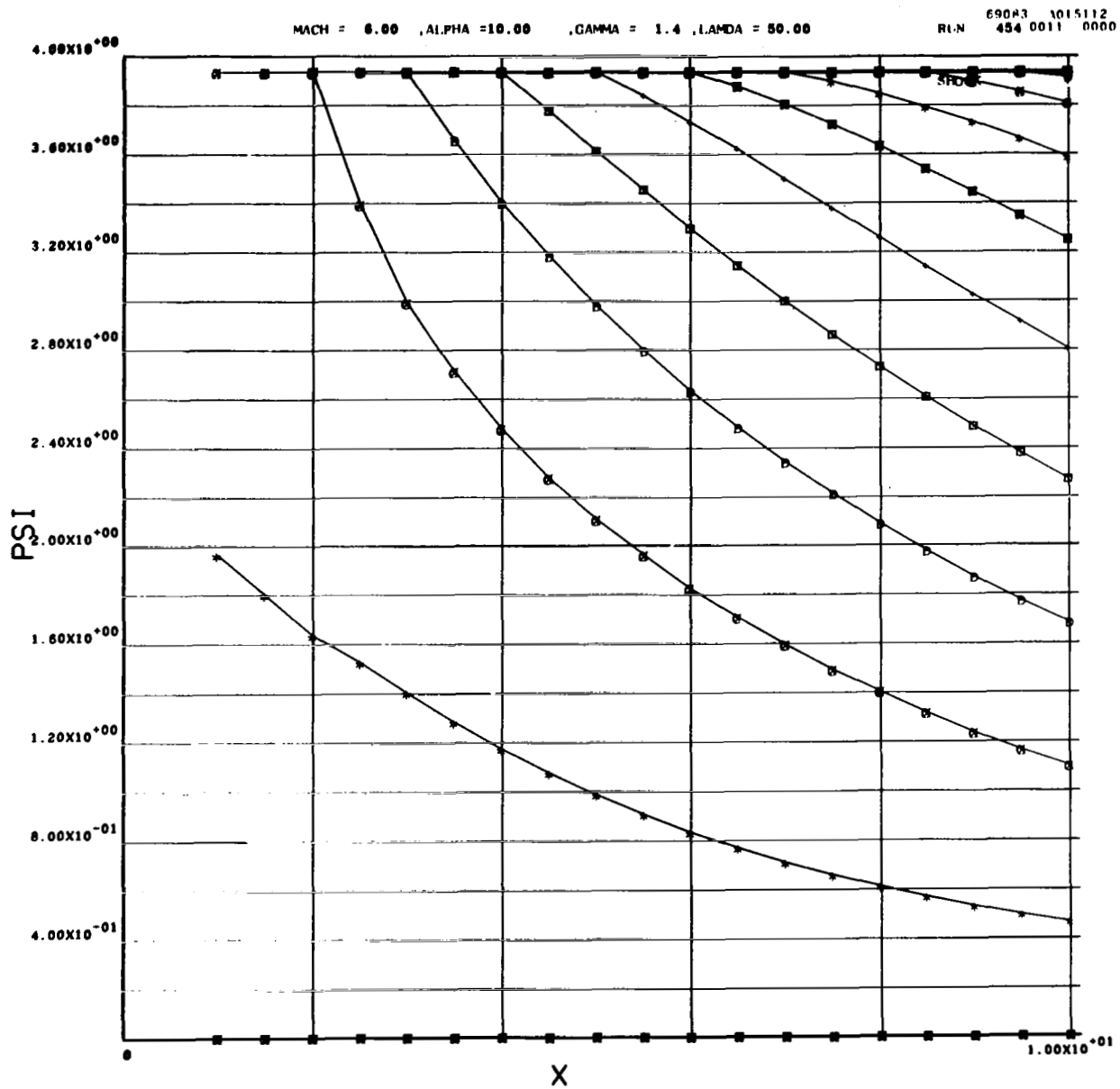


FIGURE 7. SHOCK WAVE ψ DISTRIBUTION

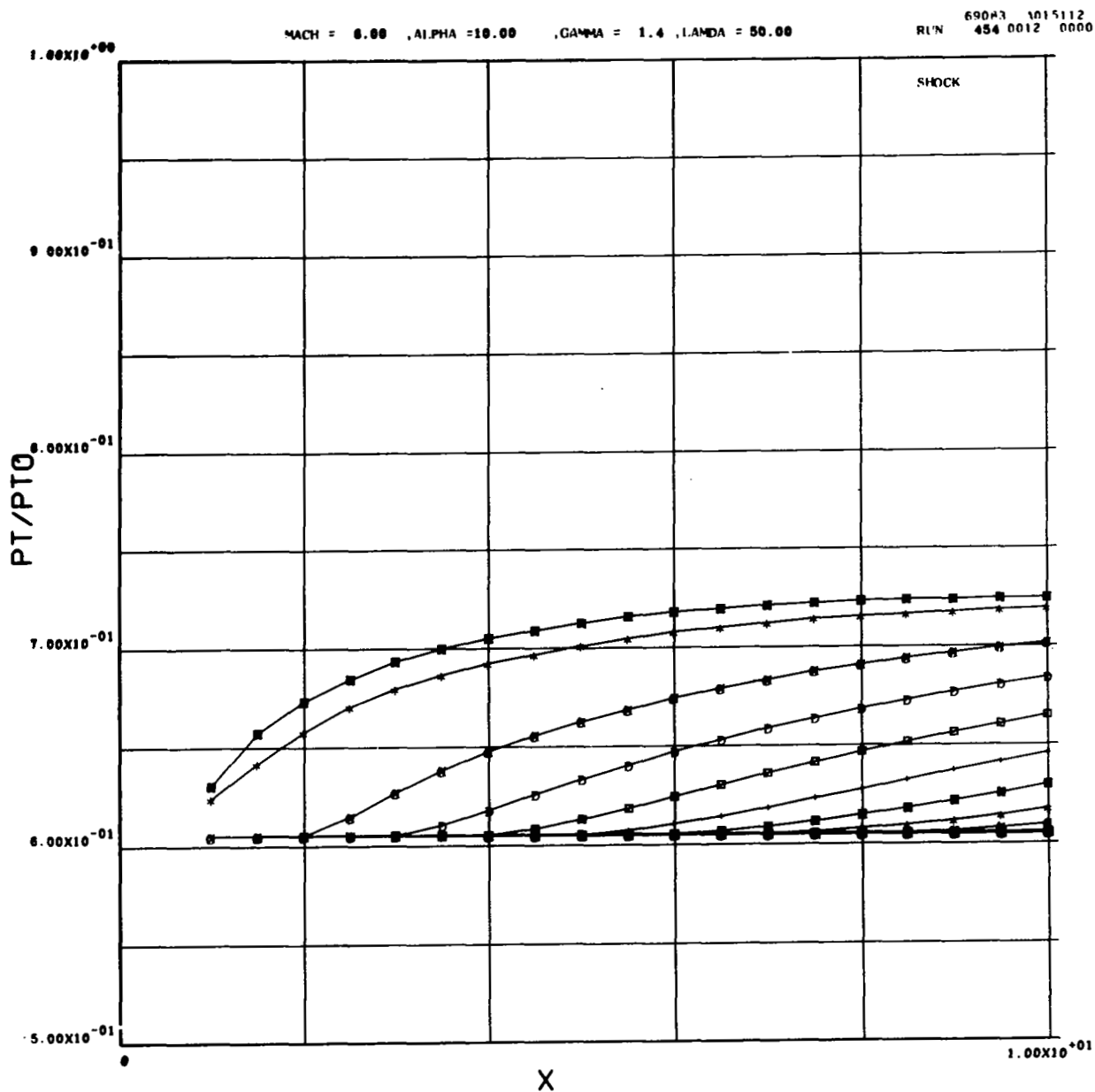


FIGURE 8. SHOCK WAVE TOTAL PRESSURE DISTRIBUTION

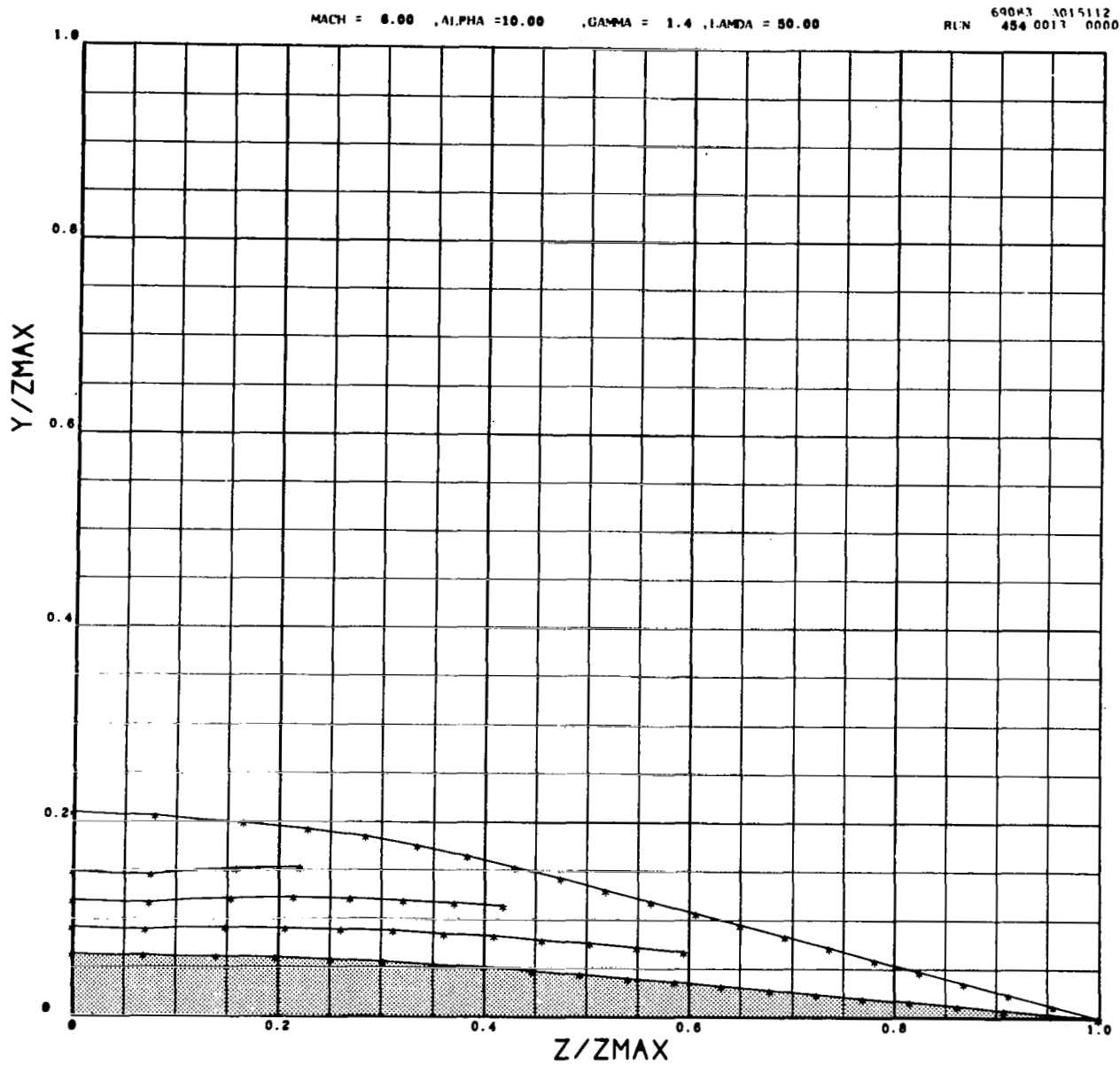


FIGURE 9. CONVERGED SOLUTION GEOMETRY

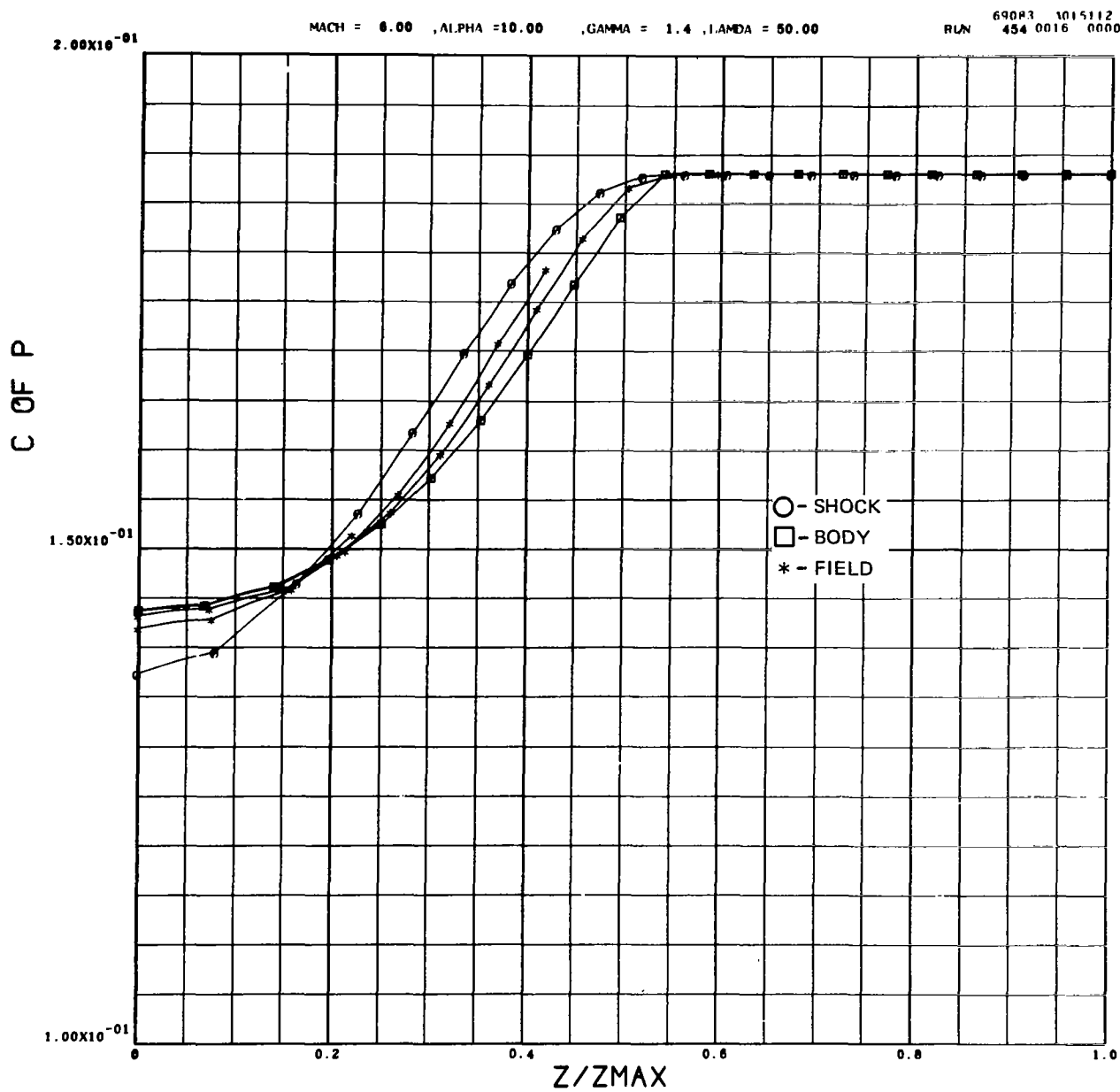


FIGURE 10. SPANWISE DISTRIBUTION OF PRESSURE

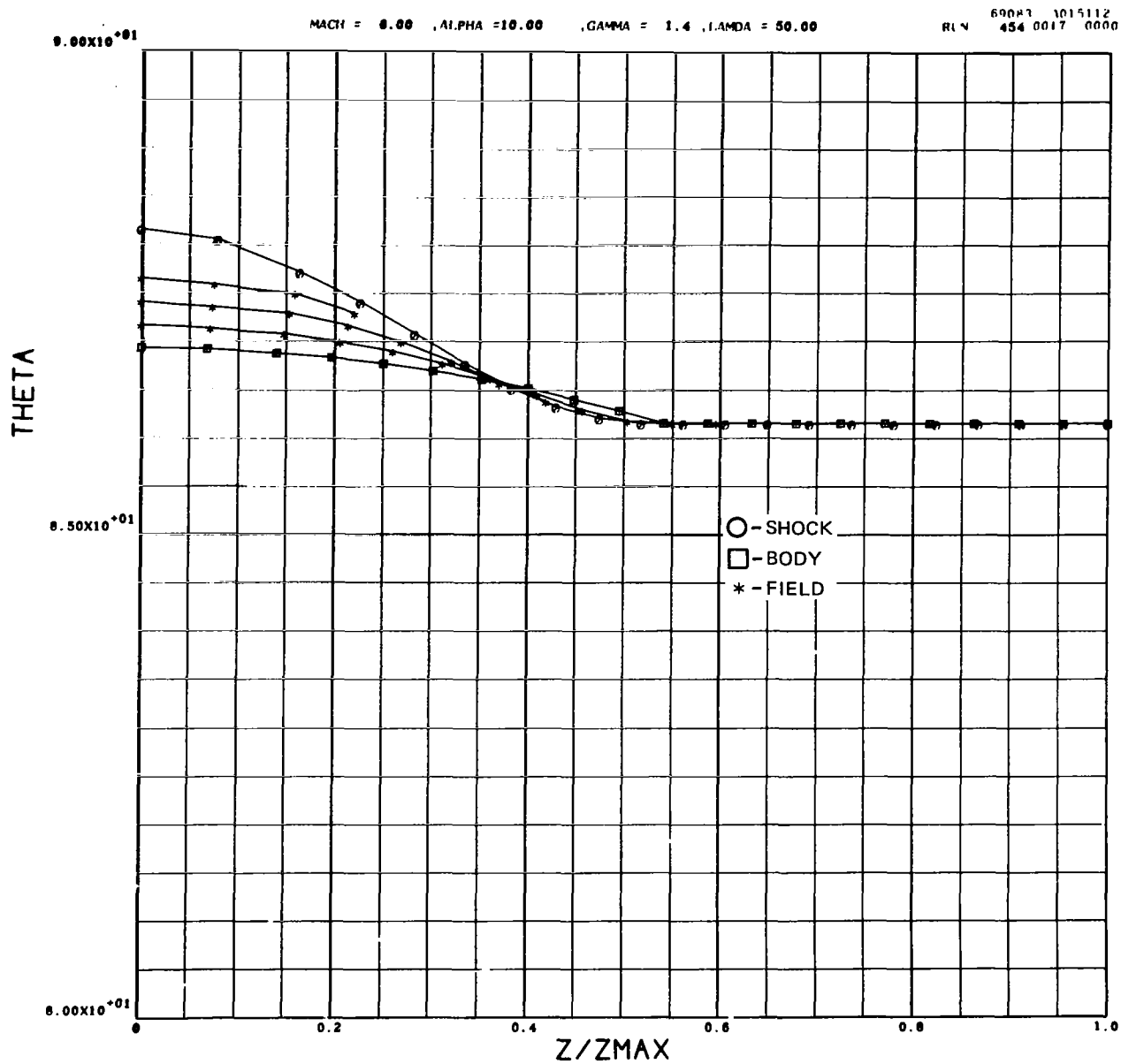


FIGURE 11. SPANWISE DISTRIBUTION OF θ

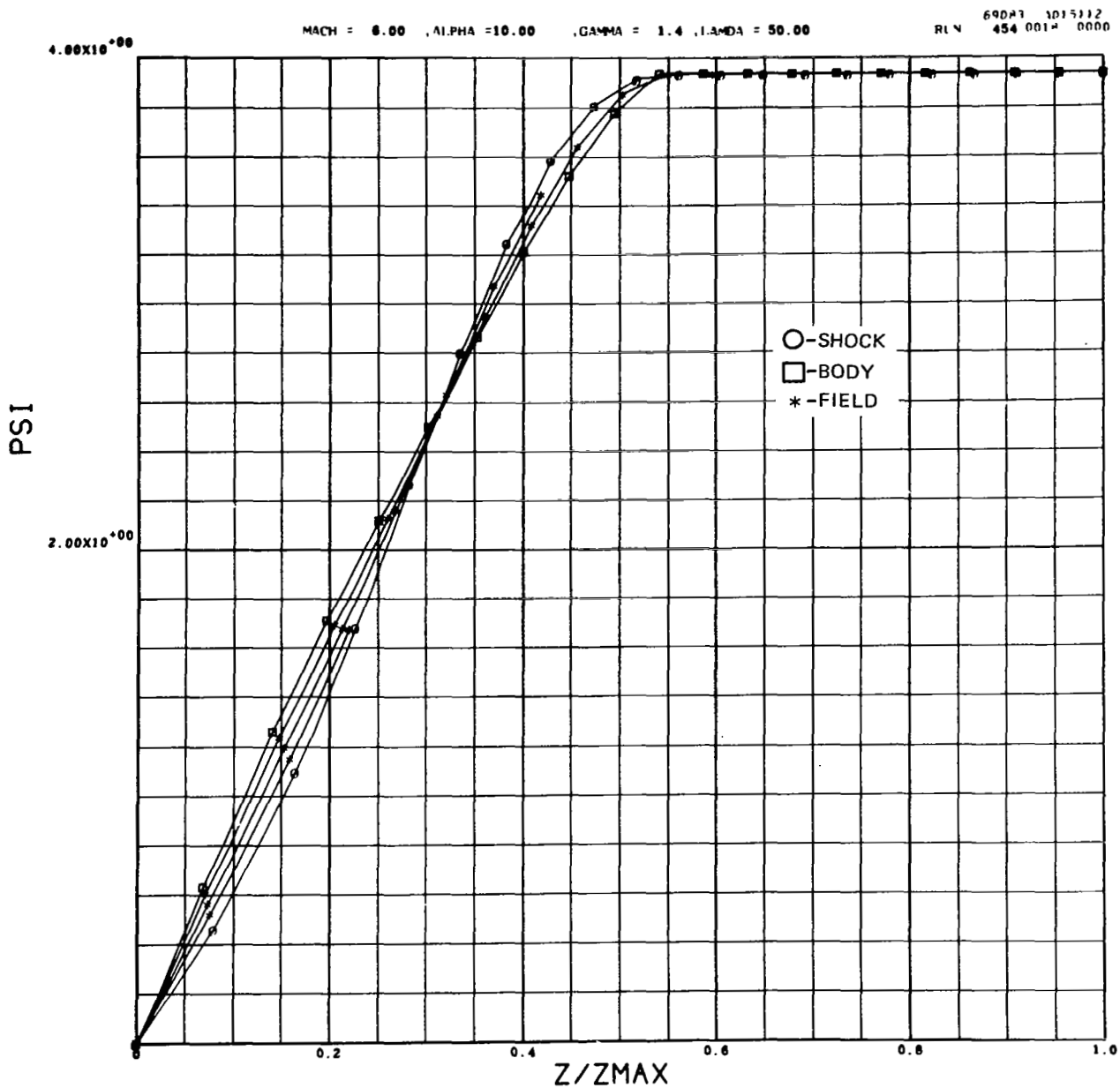


FIGURE 12. SPANWISE DISTRIBUTION OF ψ

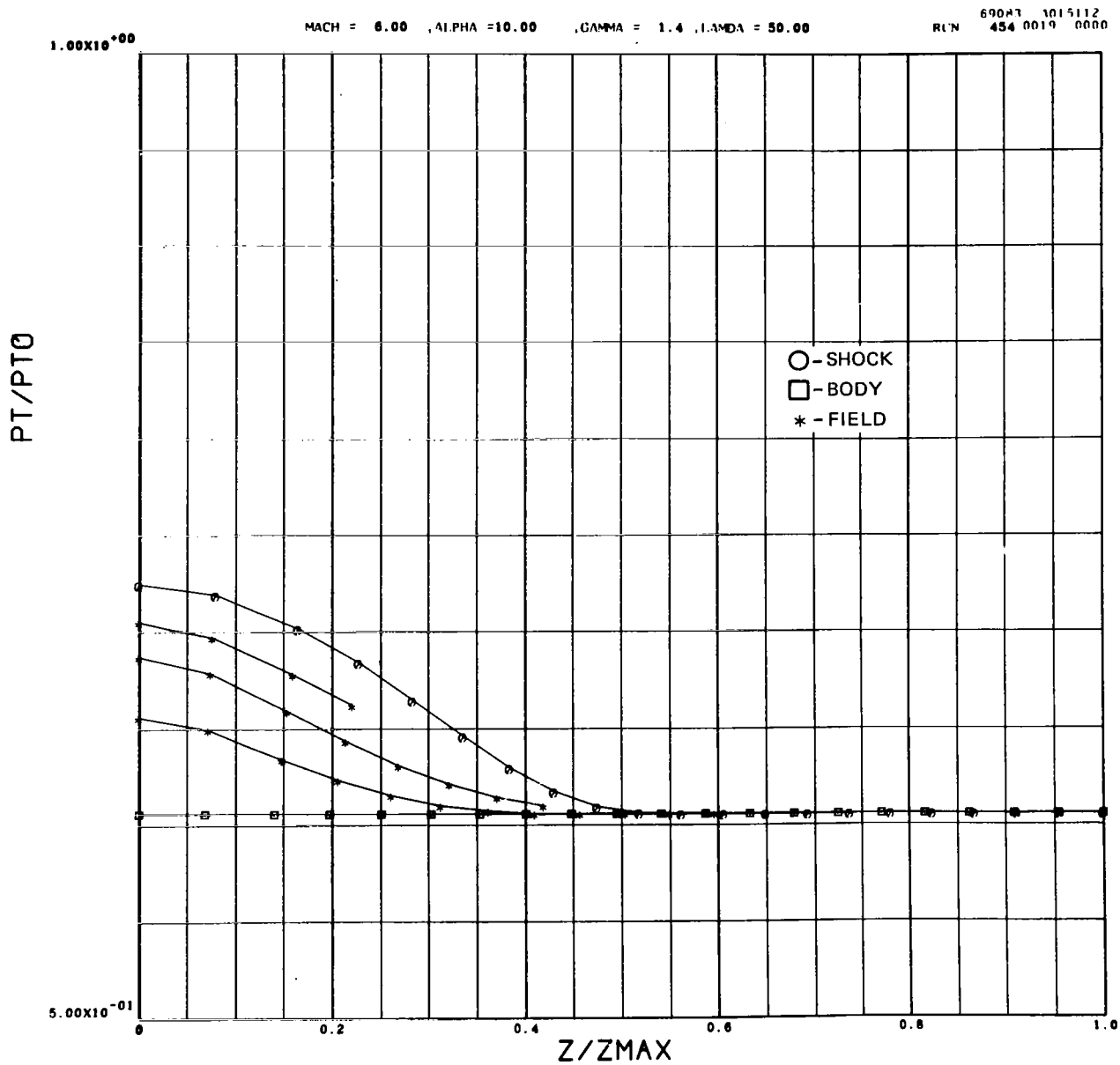


FIGURE 13. SPANWISE DISTRIBUTION OF TOTAL PRESSURE

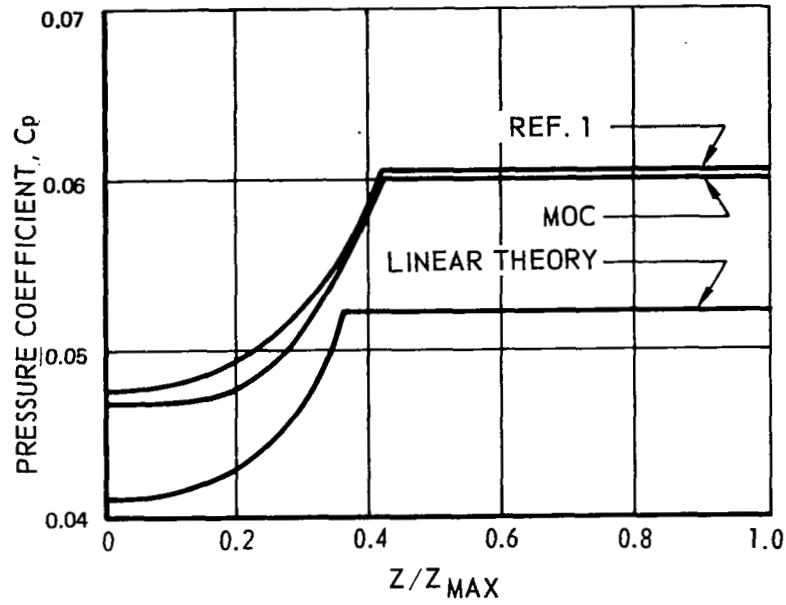


FIGURE 14. SPANWISE PRESSURE DISTRIBUTION
(FLAT PLATE, $\Lambda = 45^\circ$: $M_\infty = 3$, $\alpha = 4^\circ$)

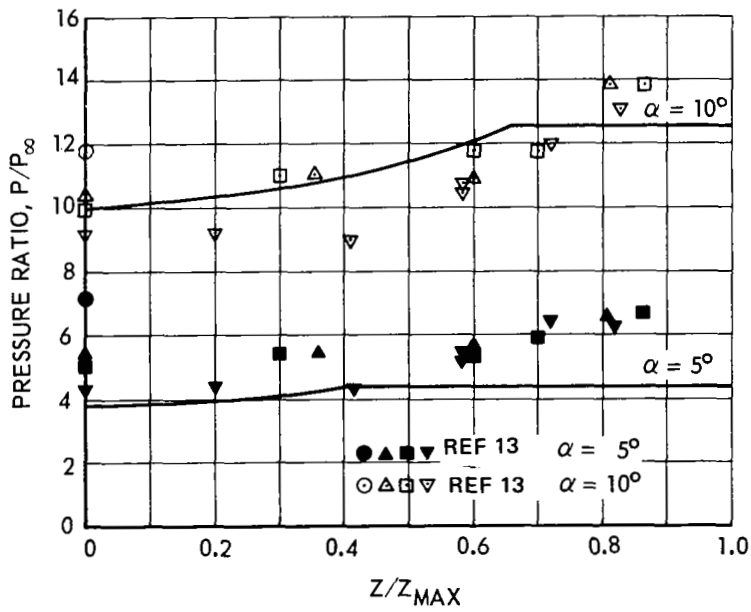


FIGURE 15. SPANWISE PRESSURE DISTRIBUTION
(FLAT PLATE, $\Lambda = 70^\circ$: $M_\infty = 11.8$, $\gamma = 1.67$)

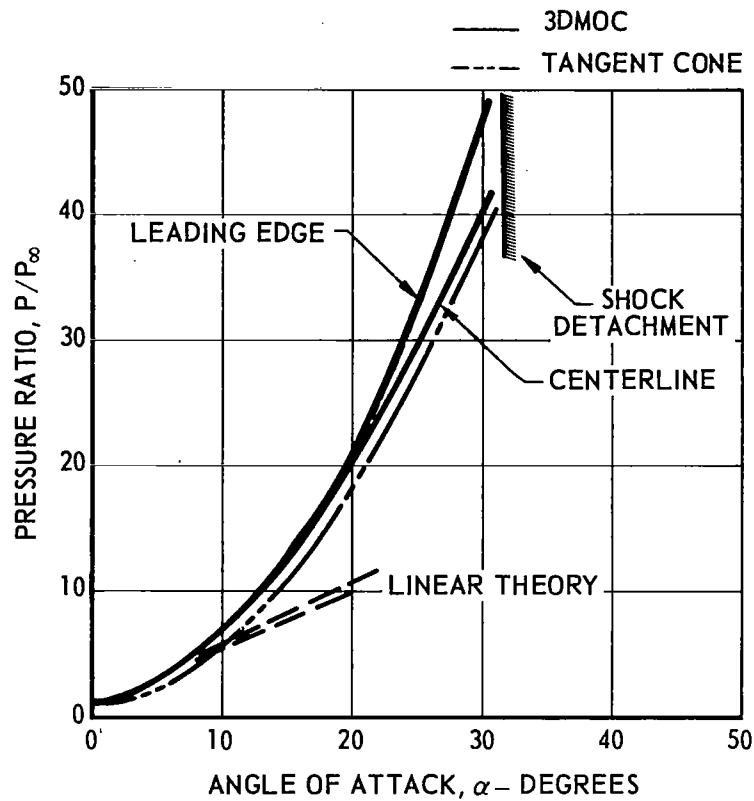


FIGURE 16. PRESSURE RATIO VS. ANGLE OF ATTACK
(FLAT PLATE, $\Lambda = 70^\circ$, $M_\infty = 11.8$, $\gamma = 1.67$)

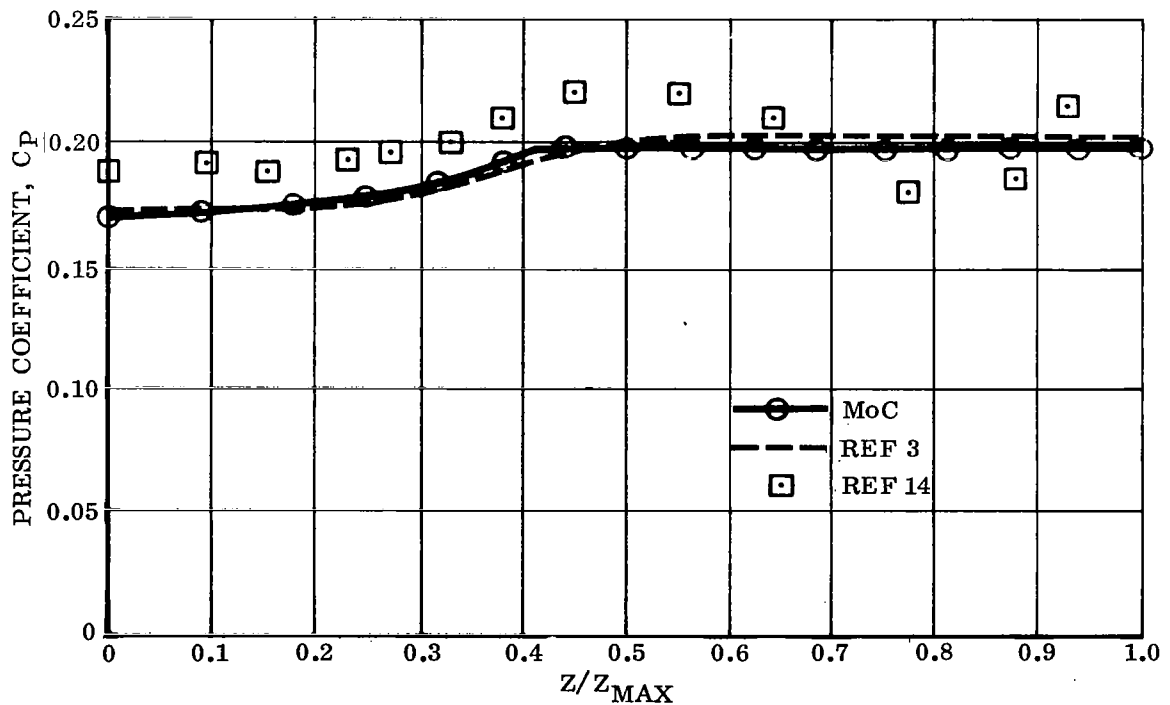


FIGURE 17. SPANWISE PRESSURE DISTRIBUTION
(FLAT PLATE, $\Lambda = 50^\circ$, $M_\infty = 5.08$, $\alpha = 14^\circ$)

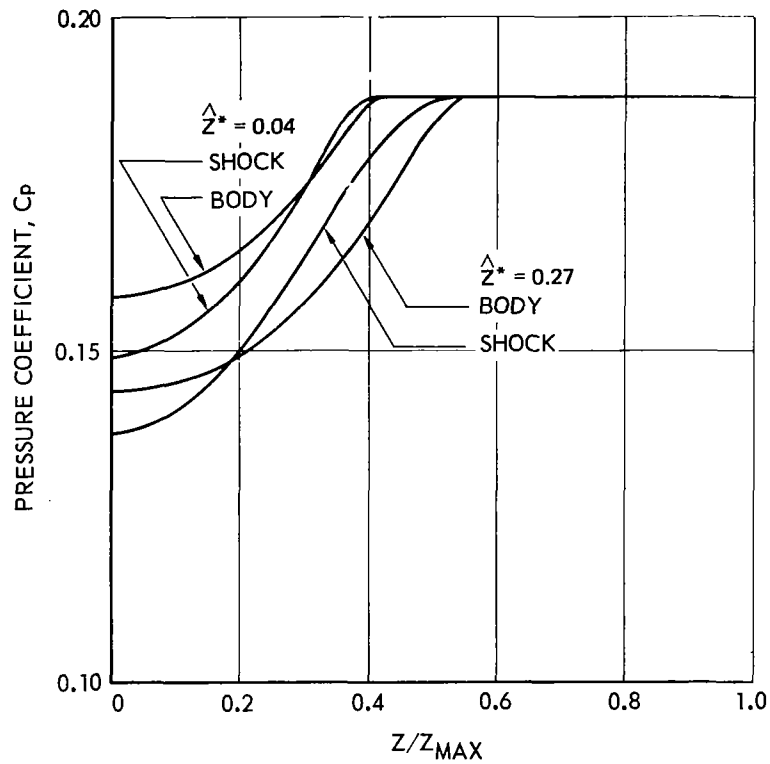


FIGURE 18. SPANWISE PRESSURE DISTRIBUTION OVER TWO MODIFIED-WEDGE SECTIONS ($\Lambda = 50^\circ$: $M_\infty = 6.0$, $\alpha = 10^\circ$)

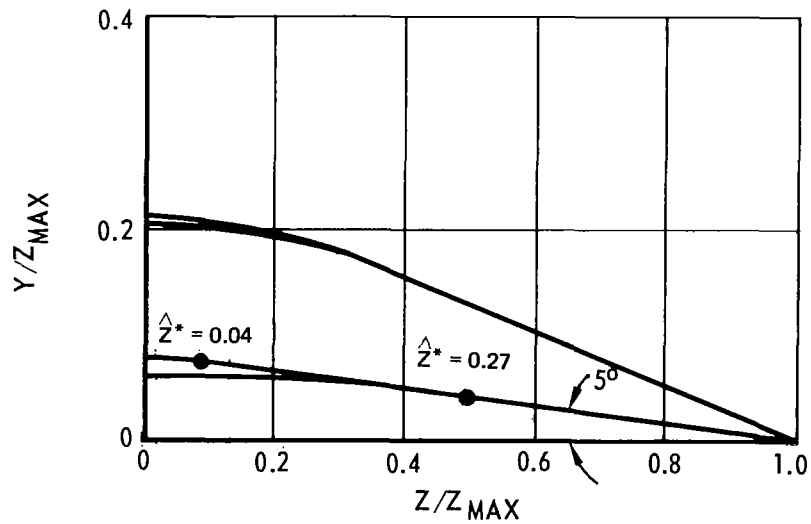


FIGURE 19. GEOMETRY AND SHOCK WAVE SHAPES FOR TWO MODIFIED-WEDGE CROSS SECTIONS ($\Lambda = 50^\circ$: $M_\infty = 6.0$, $\alpha = 10^\circ$)

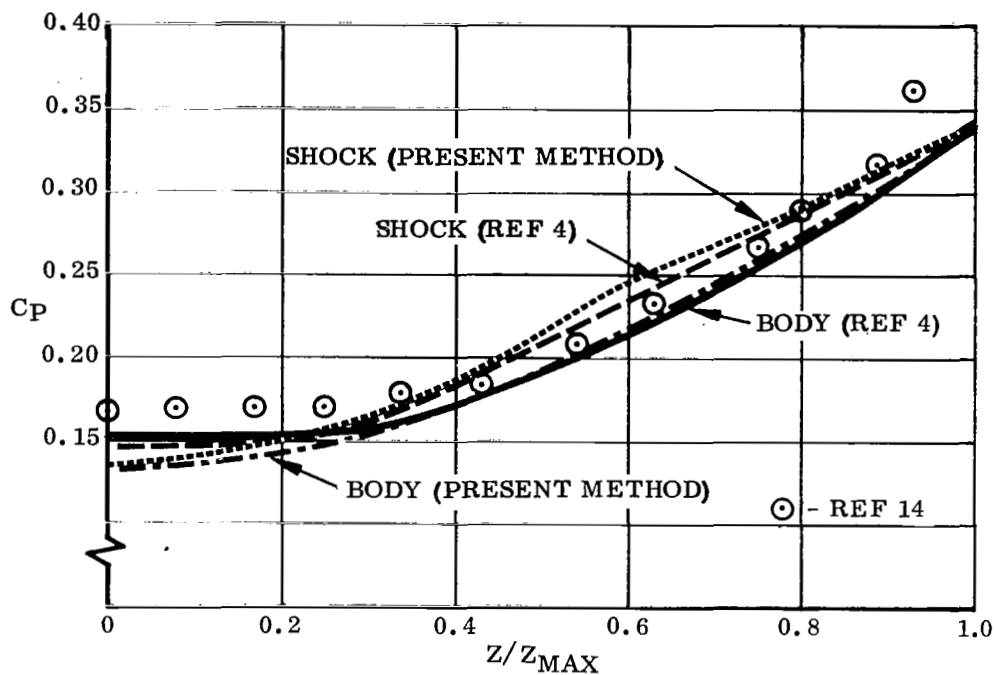


FIGURE 20. SPANWISE DISTRIBUTION ON CIRCULAR ARC WING
 $(M_\infty = 8.1, \Lambda = 50^\circ, \alpha = 10^\circ)$

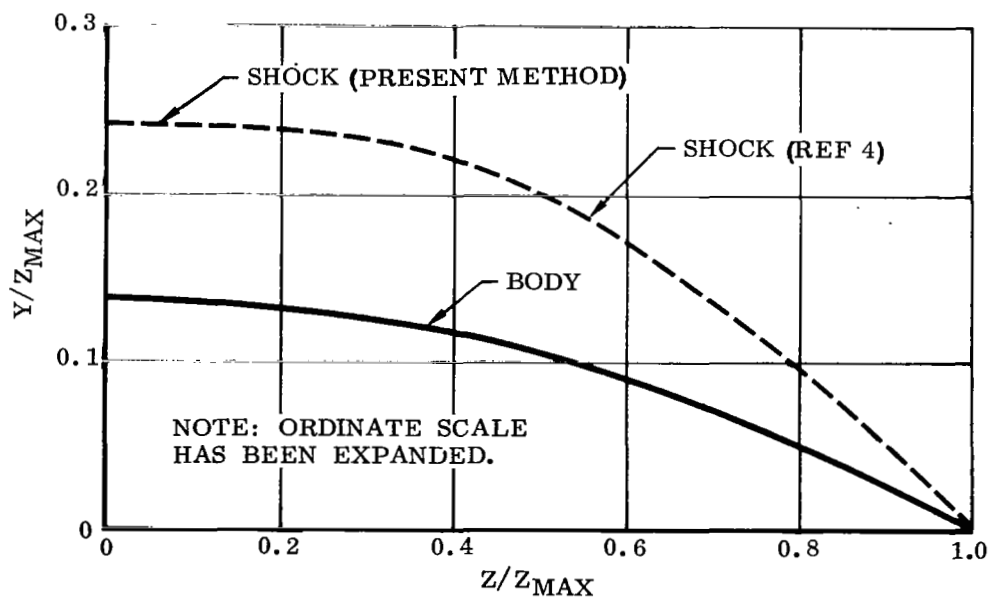


FIGURE 21. SHOCKWAVE SHAPE FOR CIRCULAR ARC WING
 $(M_\infty = 8.1, \Lambda = 50^\circ, \alpha = 10^\circ)$

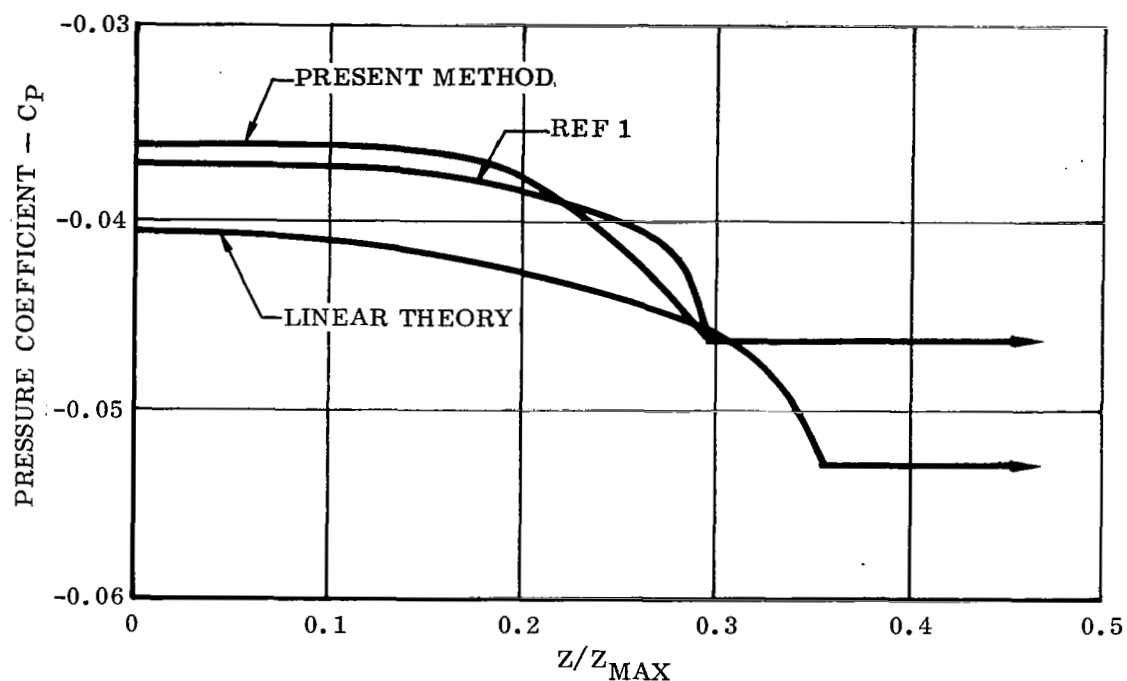


FIGURE 22. SPANWISE PRESSURE DISTRIBUTION, EXPANSION SURFACE
(FLAT PLATE, $\Lambda = 45^\circ$, $M_\infty = 3.0$, $\alpha = 4^\circ$)

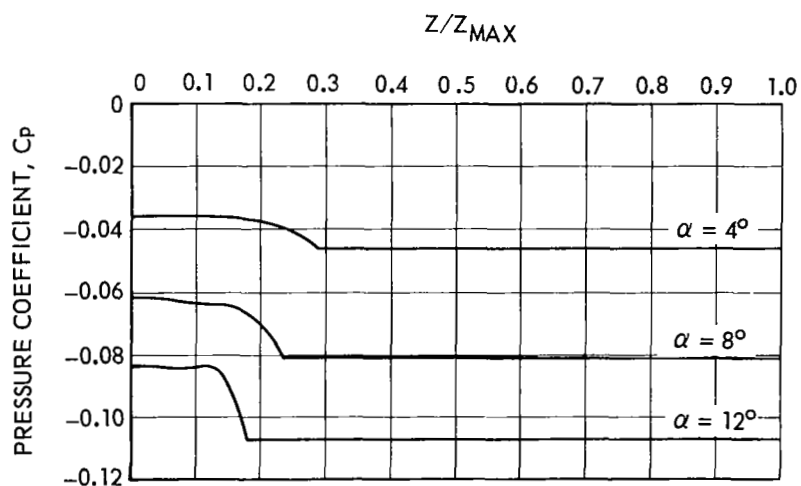


FIGURE 23. SPANWISE PRESSURE DISTRIBUTION, BY METHOD OF
CHARACTERISTICS (FLAT PLATE, $\Lambda = 45^\circ$; $M_\infty = 3.0$).

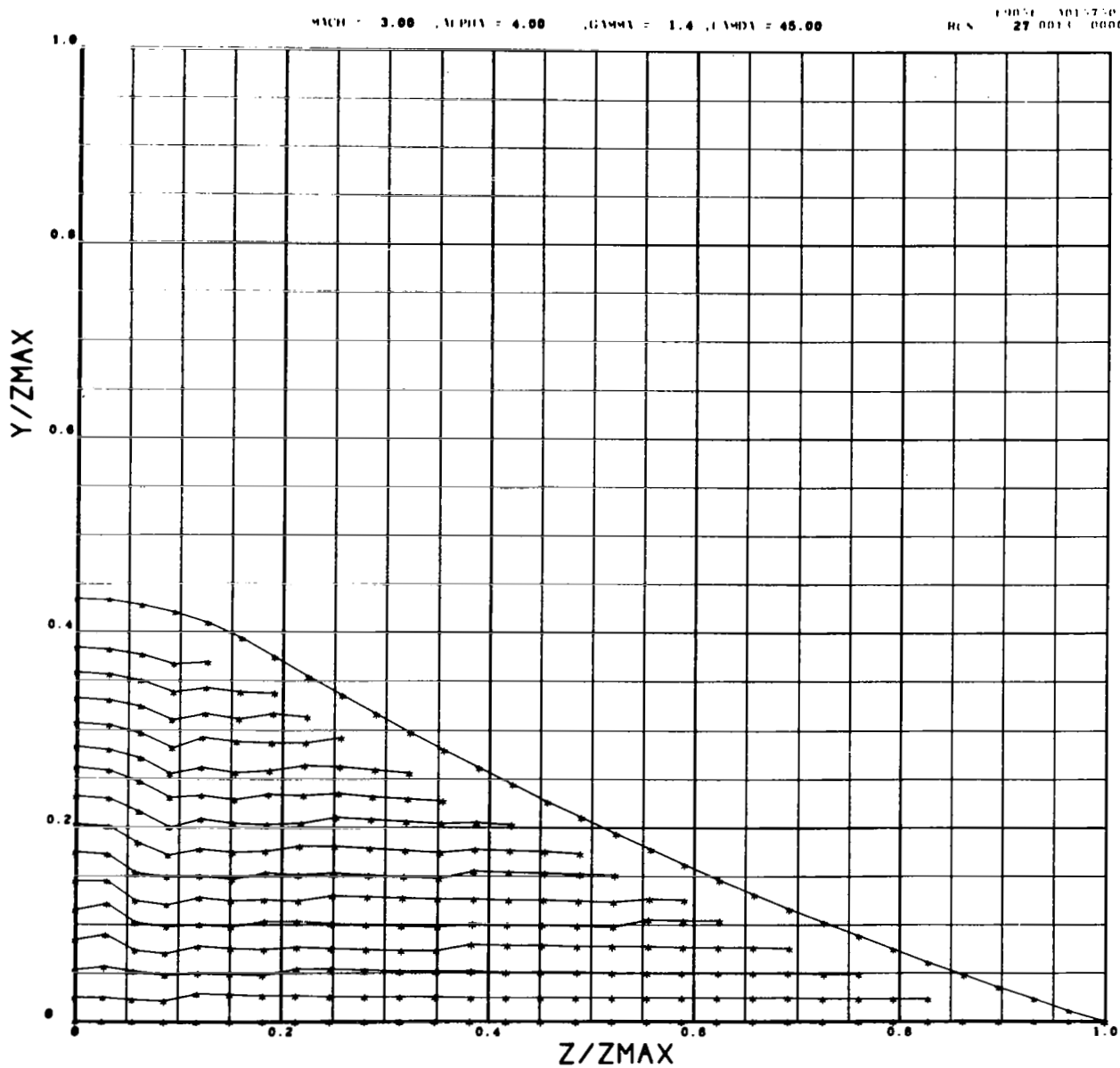


FIGURE 24. FIELD POINT LOCATION FOR FLAT PLATE EXPANSION
SURFACE SOLUTION

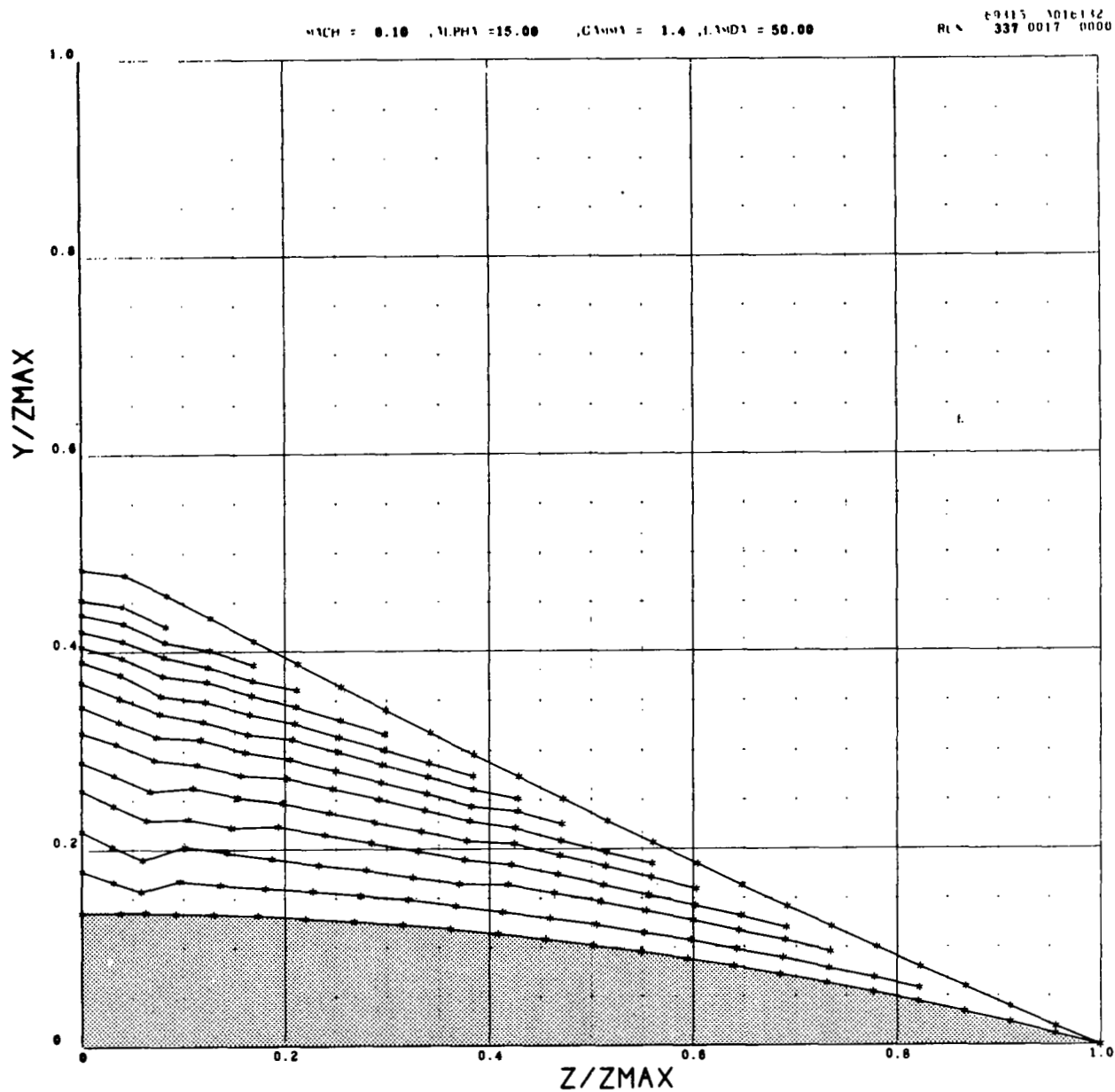


FIGURE 25. GEOMETRY OF CONVERGED SOLUTION, CIRCULAR ARC WING, EXPANSION SIDE

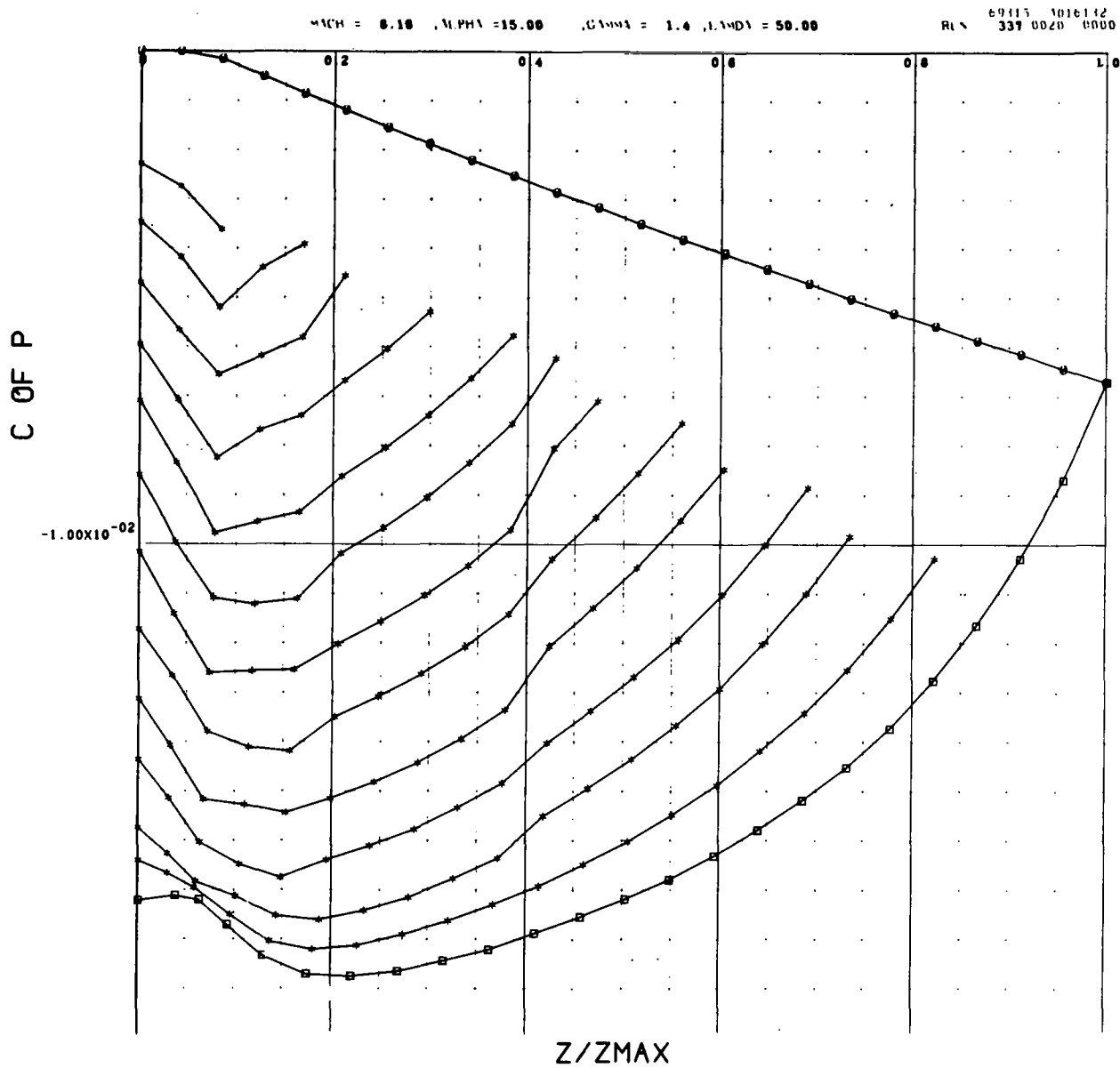


FIGURE 26. EXPANSION SIDE SPANWISE PRESSURE DISTRIBUTION
FOR CIRCULAR ARC WINGS

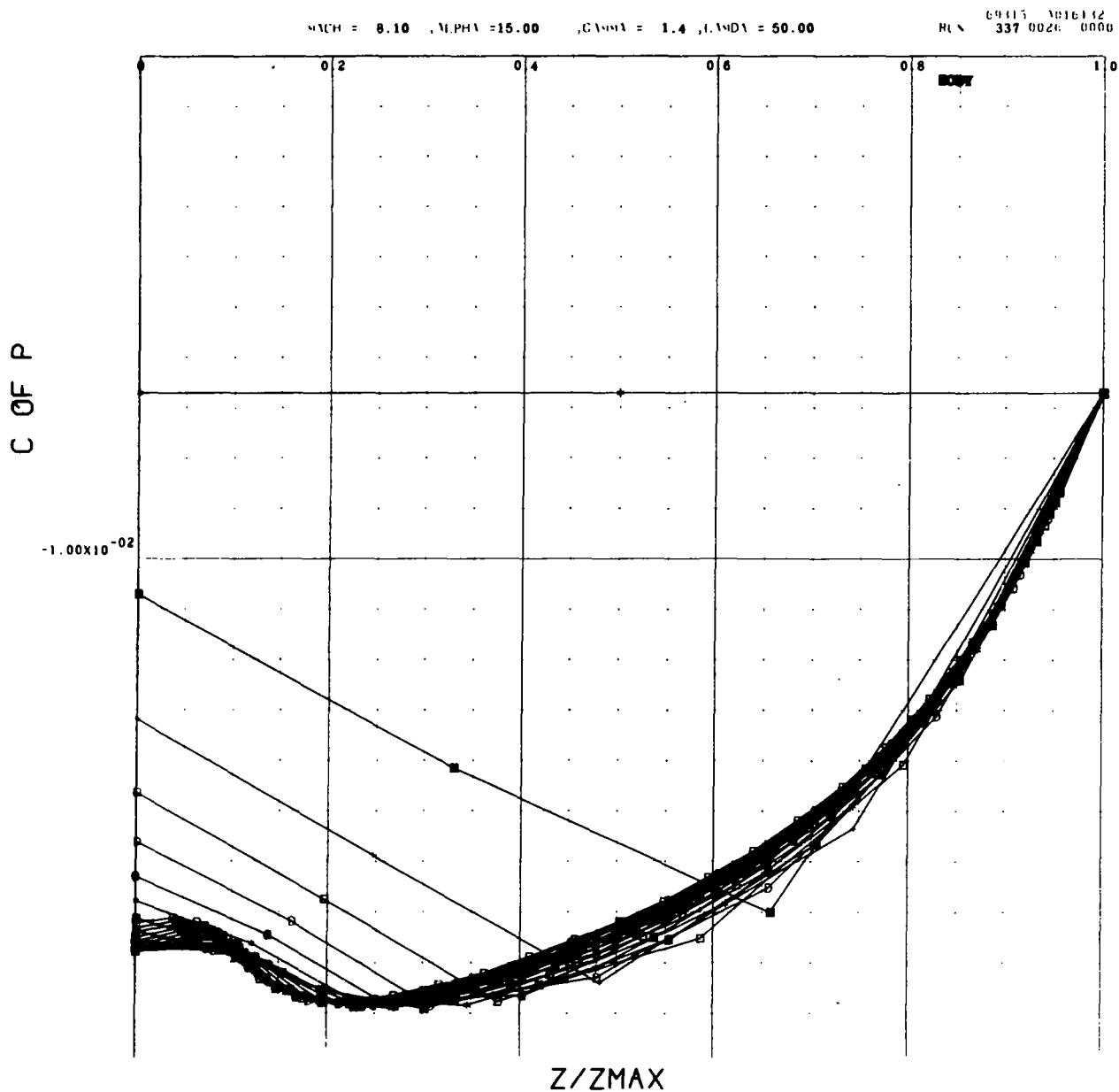


FIGURE 27. PRESSURE DISTRIBUTION CONVERGENCE FOR
EXPANSION SIDE OF CIRCULAR ARC WING